



NRL/MR/6400--10-9278

The Interaction of High-Speed Turbulence with Flames: Turbulent Flame Speed

A.Y. POLUDNENKO

E.S. ORAN

*Laboratory for Computational Physics
and Fluid Dynamics*

August 5, 2010

Approved for public release; distribution is unlimited.

REPORT DOCUMENTATION PAGE

Form Approved
OMB No. 0704-0188

Public reporting burden for this collection of information is estimated to average 1 hour per response, including the time for reviewing instructions, searching existing data sources, gathering and maintaining the data needed, and completing and reviewing this collection of information. Send comments regarding this burden estimate or any other aspect of this collection of information, including suggestions for reducing this burden to Department of Defense, Washington Headquarters Services, Directorate for Information Operations and Reports (0704-0188), 1215 Jefferson Davis Highway, Suite 1204, Arlington, VA 22202-4302. Respondents should be aware that notwithstanding any other provision of law, no person shall be subject to any penalty for failing to comply with a collection of information if it does not display a currently valid OMB control number. **PLEASE DO NOT RETURN YOUR FORM TO THE ABOVE ADDRESS.**

1. REPORT DATE (DD-MM-YYYY) 05-08-2010		2. REPORT TYPE Memorandum Report		3. DATES COVERED (From - To)	
4. TITLE AND SUBTITLE The Interaction of High-Speed Turbulence with Flames: Turbulent Flame Speed				5a. CONTRACT NUMBER	
				5b. GRANT NUMBER 64-1527-10	
				5c. PROGRAM ELEMENT NUMBER	
6. AUTHOR(S) A.Y. Poludnenko and E.S. Oran				5d. PROJECT NUMBER	
				5e. TASK NUMBER	
				5f. WORK UNIT NUMBER	
7. PERFORMING ORGANIZATION NAME(S) AND ADDRESS(ES) Naval Research Laboratory, Code 6404 4555 Overlook Avenue, SW Washington, DC 20375-5344				8. PERFORMING ORGANIZATION REPORT NUMBER NRL/MR/6400--10-9278	
9. SPONSORING / MONITORING AGENCY NAME(S) AND ADDRESS(ES) Office of Naval Research 875 North Randolph Street Arlington, VA 22203-1995				10. SPONSOR / MONITOR'S ACRONYM(S) ONR	
				11. SPONSOR / MONITOR'S REPORT NUMBER(S)	
12. DISTRIBUTION / AVAILABILITY STATEMENT Approved for public release; distribution is unlimited.					
13. SUPPLEMENTARY NOTES					
14. ABSTRACT Direct numerical simulations of the interaction of a premixed flame with subsonic, high-speed, homogeneous, isotropic, Kolmogorov-type turbulence in an unconfined system show anomalously high turbulent flame speeds, S_T . Data from these simulations are analyzed to identify the origin of this anomaly. The simulations were performed with Athena-RFX, a massively parallel, fully compressible, high-order, dimensionally unsplit, reactive-flow code. A simplified reaction-diffusion model represents a stoichiometric H_2 -air mixture under the assumption of the Lewis number $Le = 1$. Global properties and the internal structure of the flame were analyzed in an earlier paper, which showed that this system represents turbulent combustion in the thin reaction zone regime with the average local flame speed equal to its laminar value, S_L . This paper shows that: (1) Flamelets inside the flame brush have a complex internal structure, in which the isosurfaces of higher fuel mass fractions are folded on progressively smaller scales. (2) Global properties of the turbulent flame are best represented by the structure of the region of peak reaction rate, which defines the flame surface. (3) The observed increase of S_T relative to S_L exceeds the corresponding increase of the flame surface area, A_T , relative to the surface area of the planar laminar flame, on average, by $\approx 30\%$ and occasionally by as much as 50% in the course of system evolution. This exaggerated response of S_T shows that Damköhler's paradigm breaks down for sufficiently high-intensity turbulence, namely at Karlovitz numbers $Ka \geq 20$, even in the flows characterized by $Le = 1$. (4) The breakdown is the result of tight flame packing by turbulence, which causes frequent flame collisions and formation of regions of high flame curvature $\geq 1/\delta_L$, or "cusps," where δ_L is the thermal width of the laminar flame. (5) The local flame speed in the cusps substantially exceeds its laminar value, which results in a disproportionately large contribution of cusps to S_T compared with the flame surface area in them. (6) Results suggest the existence of two distinct regimes of flame evolution: the linear regime present at lower turbulent intensities when $S_T \propto A_T$, and the nonlinear regime, which is dominated by the contribution of cusps to S_T and in which S_T becomes a nonlinear function of A_T . (7) Finally, the criterion for transition to this nonlinear regime is established, and key properties and implications of this regime are discussed.					
15. SUBJECT TERMS Turbulent premixed combustion Flamelet Hydrogen Turbulence Turbulent flame speed					
16. SECURITY CLASSIFICATION OF:			17. LIMITATION OF ABSTRACT	18. NUMBER OF PAGES	19a. NAME OF RESPONSIBLE PERSON
a. REPORT	b. ABSTRACT	c. THIS PAGE			A.Y. Poludnenko
Unclassified	Unclassified	Unclassified	UL	38	19b. TELEPHONE NUMBER (include area code) (202) 767-6582

CONTENTS

1. Introduction.....	1
2. Numerical method and simulations performed.....	3
2.1. Physical and numerical models.....	3
2.2. Summary of simulations	4
3. Flame surface area and its relation to the turbulent flame speed	5
3.1. Surface area of the fuel mass fraction isosurfaces	5
3.2. Relation between S_T and $A(Y)$	6
3.3. What is the flame surface area?.....	7
3.4. Stretch factor and the balance between S_T and A_T	9
4. Flame surface density and its relation to the turbulent flame speed	10
4.1. Surface density of the fuel mass fraction isosurfaces	10
4.2. Distributions of $\bar{A}(Y)$ and $\Sigma(Y)$ and the effects of small-scale turbulence	10
4.3. Correlation between S_T and $\Sigma(Y)$	11
5. Mechanism of the turbulent flame speed increase	12
5.1. Potential causes of the increase of the local burning speed	12
5.2. Local increase of S_l in cusps formed by flame collisions	13
5.3. Structure and properties of cusps	13
5.4. Connection between the increase of S_l in cusps and S_T	15
5.5. Criterion for onset of the cusp-dominated regime of flame evolution	16
5.6. Nonlinear regime of turbulent flame evolution	17
6. Conclusions.....	19
Acknowledgments	20
Appendix A. Definition of the flame surface density.....	21
References	22
Tables	23
Figures	25

The Interaction of High-Speed Turbulence with Flames: Turbulent Flame Speed

Abstract

Direct numerical simulations of the interaction of a premixed flame with subsonic, high-speed, homogeneous, isotropic, Kolmogorov-type turbulence in an unconfined system show anomalously high turbulent flame speeds, S_T . Data from these simulations are analyzed to identify the origin of this anomaly. The simulations were performed with Athena-RFX, a massively parallel, fully compressible, high-order, dimensionally unsplit, reactive-flow code. A simplified reaction-diffusion model represents a stoichiometric H_2 -air mixture under the assumption of the Lewis number $Le = 1$. Global properties and the internal structure of the flame were analyzed in an earlier paper, which showed that this system represents turbulent combustion in the thin reaction zone regime with the average local flame speed equal to its laminar value, S_L . This paper shows that: (1) Flamelets inside the flame brush have a complex internal structure, in which the isosurfaces of higher fuel mass fractions are folded on progressively smaller scales. (2) Global properties of the turbulent flame are best represented by the structure of the region of peak reaction rate, which defines the flame surface. (3) The observed increase of S_T relative to S_L exceeds the corresponding increase of the flame surface area, A_T , relative to the surface area of the planar laminar flame, on average, by $\approx 30\%$ and occasionally by as much as 50% in the course of system evolution. This exaggerated response of S_T shows that Damköhler's paradigm breaks down for sufficiently high-intensity turbulence, namely at Karlovitz numbers $Ka \gtrsim 20$, even in the flows characterized by $Le = 1$. (4) The breakdown is the result of tight flame packing by turbulence, which causes frequent flame collisions and formation of regions of high flame curvature $\gtrsim 1/\delta_L$, or "cusps," where δ_L is the thermal width of the laminar flame. (5) The local flame speed in the cusps substantially exceeds its laminar value, which results in a disproportionately large contribution of cusps to S_T compared with the flame surface area in them. (6) Results suggest the existence of two distinct regimes of flame evolution: the linear regime present at lower turbulent intensities when $S_T \propto A_T$, and the nonlinear regime, which is dominated by the contribution of cusps to S_T and in which S_T becomes a nonlinear function of A_T . (7) Finally, the criterion for transition to this nonlinear regime is established, and key properties and implications of this regime are discussed.

Key words: Turbulent premixed combustion, Turbulence, Flamelet, Turbulent flame speed, Hydrogen

1. Introduction

One of the fundamental questions of combustion research concerns our ability to understand and predict the rate of energy release, or equivalently the speed, of the turbulent flame, which is typically the main factor controlling the evolution and dynamics of the overall system. To achieve this, two key aspects of the combustion process must be determined: (1) its local properties, namely the local speed of flame propagation, and (2) its global characteristics, i.e., the overall structure of the turbulent flame that connects the local burning velocity at each point of the flame surface with the turbulent flame speed. In general, such local and global characteristics are not universal for the combustion process. They can vary substantially both in space and time due to the unsteadiness, inhomogeneity, and anisotropy of the turbulent flow associated with the system geometry, presence of walls and boundaries, change in the flow conditions, etc.

A remarkably simple yet powerful paradigm, which suggests a description both of the local flame properties and of their connection with the turbulent flame speed, was proposed by Damköhler almost 70 years ago [1] (also see reviews by [2, 3]). Today it still remains a cornerstone of our understanding of turbulent combustion. This paradigm is formulated for a turbulent flame that is, on average, a planar, quasi-one-dimensional structure propagating in a steady, homogeneous, and isotropic turbulent flow.

According to the Damköhler's suggestion, the local flame speed, S_l , is determined only by the intensity of turbulent motions on scales smaller than the laminar flame width, δ_L . If that intensity is sufficiently low, the flame propagates at each point of its surface with the laminar flame speed, S_L . On the other hand, if small-scale motions are energetic enough, they are able to penetrate the internal structure of the flame and broaden it. Thus molecular diffusivity becomes enhanced by the turbulent transport associated with such small-scale turbulence, thereby increasing the local

flame speed, so that $S_l \sim S_L(D_T/D)^{1/2}$, where D and D_T are, respectively, the molecular and the effective turbulent diffusivities.

At the same time, the overall structure of the turbulent flame is determined by large-scale turbulent motions which stretch and fold the flame, thereby increasing its surface area, A_T . Consequently, since at each point the flame propagates with the speed S_l , the increase of the turbulent flame speed, S_T , relative to that of the planar laminar flame is equal to the increase of the flame surface area, i.e., $S_T/S_L = A_T/A_L$, where A_L is the surface area of the planar laminar flame. Therefore, in this paradigm, in order to determine S_L , it is sufficient to model only one aspect of the process of flame wrinkling and folding by turbulence, namely the resulting increase in the flame surface area.

This is essentially a kinematic model which neglects any potential feedback of the flame on the turbulent flow. At its root is one key assumption: S_l is determined only by scales $\lambda < \delta_L$, and it is constant throughout the flame surface. This implies that S_l cannot depend on the local flame geometry, i.e., flame curvature, which varies between different points of the flame surface. Consequently, S_l cannot depend on scales $\lambda > \delta_L$ that determine such local geometry. Damköhler's concept is thus, in effect, a local model, since in it the long-range velocity correlations do not affect the local properties of the combustion process. This assumption then allows one to reduce the full complexity of the three-dimensional (3D) configuration of the turbulent flame to one very simple measure – flame surface area. The result is a remarkably simple way to connect the local flame properties with the global characteristics of the turbulent flame, namely its speed.

The limitations of this assumption were known practically at the time when this model was proposed [4]. When the Lewis number $Le \neq 1$, the local flame speed can vary with the curvature of the flame. In particular, if thermal conduction is stronger than molecular diffusion, S_l will increase in concave regions of the flame and decrease in convex regions. As a result, scales $\lambda > \delta_L$ also affect S_l by stretching and folding the flame. These effects of flame strain and curvature can then be incorporated into the relation between A_T and S_T by means of the stretch factor I ([3], also see [5] for the review of the theory of flame stretch),

$$\frac{S_T}{S_L} = I \frac{A_T}{A_L}. \quad (1)$$

In principle, at this point the simplicity of the description of the turbulent flame structure is lost, since I requires knowledge not just of the flame surface area but of how the flame is actually folded inside the flame brush. Nevertheless, for the $Le = 1$ reactive mixtures, I by definition must be unity, and the details of the flame configuration should not affect the local speed of flame propagation.

Despite the broad acceptance of this picture, there are only a few studies aimed at directly verifying it. From an experimental point of view, simultaneously determining A_T and S_T in a highly turbulent flow with sufficient accuracy is associated with substantial practical difficulties. Resulting uncertainties typically do not allow robust verification of the balance between these two quantities.

Several numerical studies, however, do consider this issue. Bell et al. [6] analyzed this balance in the 3D direct numerical simulations (DNS) of the statistically planar turbulent methane flame and determined that I deviates from unity by $\lesssim 10\%$. A similar estimate was obtained by Khokhlov [7] in the 3D simulations of the Rayleigh-Taylor driven thermonuclear flames in degenerate matter. Both of these studies, however, considered reactive mixtures in which $Le \neq 1$ and, therefore, I would not be expected to be exactly equal to one. In this context, the result of [7] is particularly interesting since degenerate matter is characterized by $Le \gg 1$ and typically in excess of 10^3 . Both studies, however, did consider fairly low turbulent intensities, which precluded the formation of complex, tightly folded flame configurations. For instance, in [6], the characteristic turbulent velocity was $\approx 4.3S_L$, while in [7], it reached values $\lesssim 12S_L$. Hawkes & Chen [8] analyzed the balance between A_T and S_T in the simulations of lean statistically flat turbulent methane flames at higher turbulent intensities $\lesssim 28.5S_L$. They found the values of I generally within a few percent of unity, with the exception of the methane-hydrogen flame for which $I = 1.18$ was determined. Interpretation of the results of [8], however, is complicated by the two-dimensional nature of their simulations and by the fact that the turbulent integral scale was $< \delta_L$, which substantially suppressed flame wrinkling and prevented the formation of the tightly packed flame structure.

These studies generally support Damköhler's concept by showing that the increase in S_T is heavily dominated by the growth of A_T with the effects of the flame configuration inside the flame brush playing a minor role. They do not, however, answer the following two questions. First, while I appears to be close to unity for the $Le \neq 1$ mixtures, is I indeed exactly equal to one in the case of $Le = 1$? Since realistic reactive mixtures typically do not have $Le = 1$ exactly, this question should be understood in the sense whether $I \rightarrow 1$ as $Le \rightarrow 1$. Second, how does the value of I change with turbulent intensity? In other words, does there exist a regime in which Damköhler's concept can be expected to break down, leading to values of I substantially different from unity not only for $Le \neq 1$, but also for $Le = 1$ systems?

The last question is of particular importance since the existence of such a regime would also imply the breakdown

of flamelet models that focus on determining A_T or its volumetric equivalent, flame surface density Σ_T , in order to predict S_T . Furthermore, in such a regime the local flame speed would no longer be determined only by the small scales $\lambda < \delta_L$ but, rather, by the full turbulent spectrum. This would mark the breakdown of the locality inherent in Damköhler's model. In particular, flame propagation in this regime could no longer be considered as a local process on any scale, since the local quantity S_l would depend on the nonlocal long-range velocity correlations that potentially span the full size of the system.

The objective of this paper is to begin addressing these two questions by considering the balance between A_T and S_T in the ideally infinite, statistically planar, turbulent flame interacting with the high-speed, steady, homogeneous, isotropic turbulence. We focus on the $Le = 1$ situation to exclude thermodiffusive effects as a potential source of the non-unity values of I .

This paper continues the analysis of the simulations first presented by us in [9]. These calculations model flame interaction with turbulence of sufficiently high intensity to represent the regime that is borderline between thin and broken reaction zones, according to the traditional combustion regime diagrams [10, 11, 12] (cf. Fig. 2 in [9]). In other words, we consider the fastest turbulence which has been hypothesized to allow the existence of flamelets with the internal structure of the reaction zone essentially unaffected by the turbulent transport. The turbulent r.m.s. velocity of the flow in cold fuel is $U_{rms} \approx 35S_L$, leading to the Damköhler number $Da = 0.05$ and Gibson scale $L_G \approx 3 \times 10^{-4}\delta_L$ (Table 2).

The primary focus of [9] was a detailed study of flame properties and evolution in the presence of such high-speed turbulence. In particular, a method was presented which allowed the direct determination of the internal structure of the flame based on its actual 3D configuration inside the flame brush. The analysis showed that the preheat zone is broadened by turbulence while the reaction-zone structure remains virtually identical to that of the planar laminar flame. This study demonstrated that, even under the action of such intense turbulence, the system indeed can be robustly classified to represent the thin reaction zone regime.

The accurate determination of the reaction-zone structure in [9] showed that turbulence is not able to penetrate the flame and thus does not enhance diffusive processes. Consequently, the flame must propagate locally with the laminar speed S_L . Given that we are considering the $Le = 1$ system, this would imply that $S_T/S_L = A_T/A_L$ with a high degree of accuracy, according to Damköhler's concept.

Before the relation between S_T and A_T can be studied, however, the question of the definition of the flame surface area must first be revisited. This question, which has a seemingly simple answer at low turbulent intensities, becomes quite non-trivial in the case of a high-speed flow such as the one considered here. The flamelet structure determined in [9] is the manifestation of the fact that the ability of the turbulent cascade to penetrate the flamelet interior changes substantially from the colder parts of the flamelet in the outer preheat zone to the hotter regions in the reaction zone. One prominent consequence of this, observed in [9], was wrinkling of the turbulent flame on much smaller scales on the fuel side than on the product side. This shows that effects of turbulent motions on scales $\lambda \lesssim \delta_L$ vary significantly throughout the flamelet interior, causing varying response of its different parts to the stretching and folding action of turbulence. Therefore, the flamelet, packed into the flame brush by intense turbulence, can be expected to have a complex internal structure with the isosurfaces of different values of the fuel mass fraction, Y , or temperature, T , not being parallel to each other and, most importantly, not having the same surface area.

Our starting point in this work is thus the following question: What is the flame surface area in high-speed turbulent flows? Answering this will then allow us to determine whether there is indeed a perfect balance between the increase of the burning speed of the turbulent flame and its surface area, as suggested by Damköhler's concept, when $Le = 1$.

2. Numerical method and simulations performed

2.1. Physical and numerical models

Here we summarize the physical model, the numerical method used, and key aspects of the simulation setup. A detailed discussion can be found in [9].

We solve the system of unsteady, compressible, reactive flow equations,

$$\frac{\partial \rho}{\partial t} + \nabla \cdot (\rho \mathbf{u}) = 0, \quad (2)$$

$$\frac{\partial \rho \mathbf{u}}{\partial t} + \nabla \cdot (\rho \mathbf{u} \otimes \mathbf{u}) + \nabla P = 0, \quad (3)$$

$$\frac{\partial E}{\partial t} + \nabla \cdot ((E + P)\mathbf{u}) + \nabla \cdot (K\nabla T) = \rho q \dot{Y}, \quad (4)$$

$$\frac{\partial \rho Y}{\partial t} + \nabla \cdot (\rho Y \mathbf{u}) + \nabla \cdot (\rho D \nabla Y) = \rho \dot{Y}. \quad (5)$$

Here ρ is the mass density, \mathbf{u} is the velocity, E is the energy density, P is the pressure, Y is the mass fraction of the reactants, q is the chemical energy release, and \dot{Y} is the reaction source term. The coefficients of thermal conduction, K , and molecular diffusion, D , are

$$D = D_0 \frac{T^n}{\rho}, \quad \frac{K}{\rho C_p} = \kappa_0 \frac{T^n}{\rho}, \quad (6)$$

where D_0 , κ_0 , and n are constants, and $C_p = \gamma R / M(\gamma - 1)$ is the specific heat at constant pressure. The equation of state is that of an ideal gas. Chemical reactions are modeled using the first-order Arrhenius kinetics

$$\frac{dY}{dt} \equiv \dot{Y} = -\rho Y B \exp\left(-\frac{Q}{RT}\right), \quad (7)$$

where B is the pre-exponential factor, Q is the activation energy, and R is the universal gas constant.

Table 1 summarizes the parameters of the physical model used as well as the resulting properties of the planar laminar flame [9]. These parameters are based on a simplified reaction-diffusion model designed to represent the stoichiometric H₂-air mixture [13].

Eqs. (2)-(7) are solved using the code Athena-RFX [9] – the reactive flow extension of the magnetohydrodynamic code Athena [14, 15]. Athena-RFX is a fixed-grid, massively parallel, finite-volume, fully conservative code. It implements a variant [15] of the fully unsplit corner-transport upwind (CTU) algorithm [16] and its 3D extension presented in [17], in conjunction with the PPM spatial reconstruction [18] and the approximate nonlinear HLLC Riemann solver. Overall, the code achieves 3rd-order accuracy in space and 2nd-order accuracy in time. A detailed description and an extensive suite of tests of the hydrodynamic integration algorithm can be found in [14, 15]. Implementation of the reactive-diffusive extensions in Athena-RFX, along with the results of tests including convergence studies, is discussed in detail in [9, 19].

The simulations presented here model flame interaction with steady, homogeneous, isotropic turbulence, described by the classical Kolmogorov theory [20]. Turbulence driving is implemented using a spectral method [9, 19] similar to the one used in [21, 22]. In this method, velocity perturbations $\delta\hat{\mathbf{u}}(\mathbf{k})$ are initialized in Fourier space with each component $\delta\hat{u}_i(\mathbf{k})$ being an independent realization of a Gaussian random field superimposed with a desired energy injection spectrum. Subsequently, non-solenoidal components of $\delta\hat{\mathbf{u}}(\mathbf{k})$ are removed to ensure that $\nabla \cdot \delta\mathbf{u}(\mathbf{x}) = 0$. An inverse Fourier transform of $\delta\hat{\mathbf{u}}(\mathbf{k})$ gives $\delta\mathbf{u}(\mathbf{x})$, the velocity perturbation field in the physical space. The $\delta\mathbf{u}(\mathbf{x})$ is normalized to provide the constant rate ε of kinetic-energy injection, and the total momentum in the perturbation field is subtracted from $\delta\mathbf{u}(\mathbf{x})$ to ensure that no net momentum is added to the domain, i.e., $\int \rho \delta\mathbf{u} = 0$. Resulting velocity perturbations are added to the flow field $\mathbf{u}(\mathbf{x})$ on every time step, and the overall perturbation pattern is regenerated at every time interval $\Delta t_{vp} \approx 5\Delta x/c_s$, where c_s is the maximum sound speed in the domain.

Energy is injected only at the scale of the domain width, L , to obtain the Kolmogorov-type spectrum. The resulting turbulence is statistically steady, isotropic, and homogeneous with the inertial range of the energy cascade extending all the way to the energy injection scale (cf. Fig. 1 in [9]). Moreover, since the velocity perturbation field is divergence-free, no compressions or rarefactions are artificially induced as a result of driving.

It can be seen in eqs. (2)-(5) that we do not explicitly include physical viscosity, but instead we rely on numerical viscosity to provide the kinetic-energy dissipation. By systematically varying the resolution in this approach, the energy spectrum can be extended to progressively smaller scales $\lambda \ll \delta_L$ while maintaining the spectrum constant on larger scales. This allows us to vary the intensity only of the small-scale turbulent motions, and thus to investigate their effects by differentiating them from the effects of large scales. Such analysis also shows the range of scales which must be resolved in a numerical simulation in order to capture accurately the evolution of the turbulent flame. This is particularly important in the context of high-speed turbulent reactive flows, in which it is typically impossible to resolve the Kolmogorov scale. The analysis presented in [9] demonstrated that scales $\lambda \ll \delta_L$ have virtually no effect on the properties of the turbulent flame with the exception of the degree of flame surface wrinkling on the fuel side. This showed that the evolution of the turbulent flame can be accurately reproduced without the need to resolve scales $\lambda \ll \delta_L$. We refer to [9] for the detailed discussion of this issue and, in particular, for the discussion of the applicability of the obtained results to the actual stoichiometric H₂-air mixture.

2.2. Summary of simulations

Key parameters of the simulations discussed here are summarized in Table 2. The main difference between the three calculations is the resolution, which progressively increases from $\Delta x = \delta_L/8$ in S1 to $\Delta x = \delta_L/32$ in S3. The domain in all cases was initialized with uniform density ρ_0 and temperature T_0 (see Table 1). In S1 and S2, initial fluid velocities were set to 0. In contrast, the velocity field in S3 was initialized with the ideal energy spectrum $\mathcal{E}(k) \propto k^{-5/3}$ extending from the energy injection scale L to the numerical Kolmogorov scale $\eta = 2\Delta x$. This initial spectrum was normalized to ensure that at $t = 0$ the total kinetic energy in the domain was equal to its predicted steady-state value as described in [19]. In S1 and S2, the flow field was allowed to evolve for the time $t_{ign} = 3\tau_{ed}$, and in S3 for the

time $t_{ign} = 2\tau_{ed}$, to develop the steady-state turbulent flow field. At the time t_{ign} , a planar laminar flame with its front parallel to the x - y plane¹ was initialized in the domain with the values of ρ , T , and Y based on the exact laminar flame solution. The velocity field was not modified, thereby preserving the structure that developed during the equilibration stage.

Prior to t_{ign} , all domain boundaries are periodic. At t_{ign} , boundary conditions (BCs) along the left and right z -boundaries are switched to zero-order extrapolation in order to prevent pressure build-up inside the domain and to accommodate the resulting global fluid flow. Reflections of the acoustic perturbations caused by such BCs can be neglected in comparison with the acoustic noise generated by the turbulent flow field itself, and overall such choice of the BCs was found not to introduce any unphysical artifacts and thus not to affect the solution accuracy. Furthermore, any potential effect of the outflow BCs was minimized by the large length-to-width ratio of the computational domain, which allowed us to keep the flame brush sufficiently far from the boundaries at all times [9]. Hereafter, for simplicity we refer to the moment of ignition as $t = 0$.

Energy is injected into the domain with the constant rate ε per unit volume for the total duration of the simulations to provide steady driving of the turbulent flow. The value of ε was chosen to produce a high-intensity turbulence field that, however, was weak enough to minimize the probability of creating weak transonic shocklets arising from the intermittency in turbulent flow. The characteristic turbulent velocities and the turbulent integral scale of the steady-state flow prior to the moment of ignition are listed in Table 2. Corresponding values of the Damköhler number and the Gibson scale, given in the table, show that $Da \ll 1$ and $L_G \ll \delta_L$. Prior analysis of the resulting structure of the turbulent flame demonstrated that, despite the high turbulent intensity, small-scale turbulence fails to penetrate the internal structure of the flame and the system evolves in the thin reaction zone regime [9].

Detailed discussion of the turbulent flame evolution in the simulations is given in [9]. Here, for completeness, we reproduce in Fig. 1 the time histories of the flame-brush width, δ_T , normalized by δ_L , as well as S_T , normalized by S_L , (see Fig. 4 in [9]) for all three calculations, since these two quantities are used extensively in this work.

The width of the turbulent flame brush is defined as

$$\delta_T = z_{1,max} - z_{0,min}, \quad (8)$$

where $z_{0,min}$ and $z_{1,max}$ are defined as

$$\begin{aligned} z_{0,min} &= \max(z) : Y(x, y, z) < 0.05 \quad \forall (x, y, z < z_{0,min}), \\ z_{1,max} &= \min(z) : Y(x, y, z) > 0.95 \quad \forall (x, y, z > z_{1,max}). \end{aligned} \quad (9)$$

In other words, $z_{0,min}$ marks the rightmost x - y -plane to the left of which is pure product, while $z_{1,max}$ marks the leftmost x - y -plane to the right of which is pure fuel. This is illustrated in Fig. 2. The turbulent flame speed is defined as

$$S_T = \frac{\dot{m}_R}{\rho_0 L^2}, \quad (10)$$

where \dot{m}_R is the total rate of fuel consumption inside the flame brush, i.e., the total mass of reactants which is transformed to product per unit time. The detailed discussion of this choice of the definition of S_T can be found in [9].

Finally, Table 3 lists the time-averaged values of both δ_T/δ_L and S_T/S_L [9] as well as of other key characteristics of the turbulent flame discussed below. Table 3 also shows the corresponding order of self-convergence for each quantity listed. Since the computational cell size decreases progressively by a factor of 2 for each simulation, the order of self-convergence $O(\phi)$ of a variable ϕ is defined as

$$O(\phi) = \log_2 \left(\frac{|\phi_{S1} - \phi_{S3}|}{|\phi_{S2} - \phi_{S3}|} \right). \quad (11)$$

3. Flame surface area and its relation to the turbulent flame speed

3.1. Surface area of the fuel mass fraction isosurfaces

Fig. 3a,b shows the evolution of the surface areas $A_{0.01}$ and $A_{0.99}$ of the fuel mass fraction isosurfaces of $Y = 0.01$ and $Y = 0.99$, respectively. We use the notation $A_Y \equiv A(Y = Y')$, and all isosurfaces are constructed using the ‘‘marching cubes’’ algorithm. These isosurfaces represent two outer boundaries of the flame brush, separating it from pure product and pure fuel. All values are normalized by the domain cross-section L^2 corresponding to the surface area

¹The longest dimension of the domain is along the z -axis.

of the planar laminar flame unperturbed by turbulence. In principle, the normalization should be performed over some average surface area of the flame brush, thus reflecting its overall large-scale shape. With sufficiently good accuracy, however, the turbulent flame in the system considered here can be viewed, on average, as a planar propagating front, and thus we normalize over its area L^2 .

Fig. 3a shows that $A_{0,01}$ exhibits substantial variability, similar to δ_T and S_T (cf. Fig. 1). There is a clear correspondence between the peaks and troughs in the values of $A_{0,01}$ and S_T and, to a lesser extent, δ_T . Moreover, in a manner similar to δ_T and S_T , $A_{0,01}$ shows less variability with increasing resolution, and it appears on average to have converged.

Such manifest correlation in the behavior of $A_{0,01}$ and S_T is the reflection of the evolutionary cycle of the flame brush, discussed in [9]. It was shown that in the turbulent flame, which on average is in a steady state, the influx of fresh fuel and the rate of its consumption never perfectly balance each other. Instead, periodically either one or the other process dominates. In particular, an increase in the flame surface area inside the brush, and the associated increase in δ_T , leads to a higher S_T . This causes rapid consumption of fuel inside the brush, decreasing both the flame surface area and the overall width of the flame brush. As a result, a slower, less convolved flame emerges, which is thus more susceptible to the action of turbulence. This leads to increased folding and stretching of the flame, and the cycle repeats.

The behavior of $A_{0,99}$ is pronouncedly different. There appears to be no correlation between variations in $A_{0,99}$ and either δ_T or S_T . Moreover, with increasing resolution, the magnitude of the variations increases, and there is no evidence of convergence of the growing average values of $A_{0,99}$. We will consider the correlation between $A(Y)$ and both S_T and δ_T in a more quantitative form in § 3.3.

These conclusions regarding the change of $A_{0,01}$ and $A_{0,99}$ with resolution are supported by Fig. 3c, which shows the full normalized time-averaged distributions $\bar{A}(Y)/L^2$ for all values of Y . In simulation S1, $\bar{A}_{0,01}$ and $\bar{A}_{0,99}$ are nearly equal. With increasing resolution, however, they diverge to the point that, in S3, there is almost a factor of 2 difference between them. Values of $\bar{A}_{0,01}$ steadily decrease and they indeed demonstrate convergence. At the same time, $\bar{A}_{0,99}$ increases with resolution, and the difference between S2 and S3 is only marginally smaller than between S1 and S2.

This behavior is part of a broader qualitative change in the overall shape of the distribution of \bar{A} which occurs around $Y \approx 0.5$, i.e., at the boundary of the reaction and preheat zones. The lower resolution of S1 suppresses small-scale turbulent motions, which, in turn, causes less flame wrinkling in the preheat zone. As a result, the flame-brush surface appears similar both on the product and fuel sides (cf. Fig. 3 in [9]). With higher resolution, however, turbulent flame wrinkling becomes more pronounced with increasing distance from the reaction zone, and the distribution of \bar{A} develops a distinctive inverted-S shape. The consequence of this was observed in [9] (see Fig. 3 therein), which showed a much more highly convolved flame-brush surface on the fuel side in calculations S2 and S3. We will discuss the role of small-scale turbulence in further detail in § 4.2.

Profiles of \bar{A} in S2 and S3 are closer to each other in the reaction zone than in the preheat zone. Table 3 shows that in the region of peak reaction rate, i.e., at $Y \approx 0.15$, $\bar{A}(Y)/L^2$ exhibits the 3rd-order convergence. This is substantially faster than what would be expected for an overall 2nd-order-accurate code. Moreover, in all three calculations, \bar{A} varies the slowest inside the reaction zone, i.e., for $Y \approx 0.15 - 0.5$. This shows that isosurfaces of the fuel mass fraction, on average, follow each other closely within the reaction zone, which is thus folded and stretched by turbulence as a coherent structure. This is in agreement with the very low variability in the reaction zone of the instantaneous profiles of Y and T , which represent the internal flamelet structure [9].

3.2. Relation between S_T and $A(Y)$

Results presented in § 3.1 demonstrate that the flamelet, folded inside the turbulent flame by high-intensity turbulence, has a complex internal structure with a distinctly different response of its various parts to the action of turbulence. Consider the modified eq. (1)

$$\frac{S_T}{S_L} = I \frac{A(Y)}{L^2}, \quad (12)$$

in which the surface area of the turbulent flame A_T is now represented by the isosurface area $A(Y)$, and we set the surface area of the planar laminar flame A_L equal to the domain cross-section area L^2 . Using data for $A(Y)$ and S_T , eq. (12) then allows us to assess the extent to which Damköhler's concept is valid in the regime modeled in our simulations. Since A is not a constant, however, but rather it depends on the choice of Y , I now also, formally, becomes a function of Y .

As an example, Fig. 4a shows the evolution of the stretch factor $I_{0,15} \equiv I(Y = 0.15)$ based on the area of the isosurface that corresponds to the peak reaction rate in the flame. Even though it is fairly constant on average, $I_{0,15}$ exhibits quite strong variability. In all three simulations and at all times after the flame has reached its quasi-steady state, $I_{0,15}$ remains above unity becoming as high as 2.0 in S1 and 1.5 in S3. Similarly to other quantities we have considered, $I_{0,15}$ shows less variability with increasing resolution. Time-averaged values of $I_{0,15}$ are given in Table 3.

In particular, $\bar{I}_{0.15} = 1.30$ in S3, and this value can be viewed as converged to within a few percent with the overall rate of convergence being somewhat faster than linear.

In order to assess the dependence of I on the choice of the value of Y , consider the time-averaged distributions of $I(Y)$ shown in Fig. 4b. In particular, we show $\bar{I}(Y) = (\overline{S_T/S_L})/(\overline{A_T(Y)}/L^2)$.² In all simulations, \bar{I} is substantially larger than unity throughout the reaction zone. Also, $\bar{I} > 1.0$ for all values of Y , with the only exception being the outermost region of the preheat zone in S3, where $\bar{I} < 1.0$ for $Y \gtrsim 0.93$. In the higher resolution simulations S2 and S3, \bar{I} decreases monotonically with increasing values of Y . Similarly to \bar{A} , \bar{I} varies the least inside the reaction zone, i.e., for $Y \approx 0.15 - 0.5$. For example, the difference between $\bar{I}_{0.15}$ and $\bar{I}_{0.5}$, which corresponds to the boundary between the reaction and preheat zones, is $\approx 2\%$ in S1, $\approx 5\%$ in S2, and $\approx 8\%$ in S3.

Finally, the $\pm\sigma$ standard deviation of individual values of $I(Y)$ in S3 is shown in Fig. 4b as a shaded gray area. The σ is the smallest in the reaction zone, where it is $\lesssim 15\%$ of \bar{I} . It becomes $> 30\%$ in the preheat zone as a result of the stronger variability of A at large values of Y (cf. Fig. 3). Note that throughout the reaction zone, i.e., for $Y \lesssim 0.5$, the $\bar{I} \pm \sigma$ interval is above unity.

3.3. What is the flame surface area?

Distributions of the time-averaged stretch factor \bar{I} , shown in Fig. 4b, fail to answer the question concerning the validity of Damköhler's concept in the regime considered here. Large values of \bar{I} , found in the reaction zone, indicate a significant departure from Damköhler's model. At the same time, values of \bar{I} close to unity, present in the outer regions of the preheat zone, suggest that the increase in S_T can be completely accounted for by the increase in A .

This demonstrates the importance of the question previously raised in § 1: What is the surface area of the flame in such high-speed turbulent flows? In particular, since the response of different parts of the flamelet to the action of intense turbulence is pronouncedly distinct, what value of Y most fully and accurately represents the overall behavior of the turbulent flame?

These questions can be addressed by considering the correlation of $A(Y)$ with two global properties of the turbulent flame, its speed and width. Fig. 5 shows correlations between S_T/S_L and $A(Y)/L^2$ calculated for three representative values of Y : $Y = 0.15$, corresponding to the region of peak reaction rate, $Y = 0.5$, corresponding to the boundary between the reaction and the preheat zones, and $Y = 0.95$, corresponding to the coldest part of the preheat zone. The left panels of Fig. 5 show the time-evolution of all quantities, while the right panels show the corresponding correlation scatter plots.

Since both the local flame speed and the induction times of the unburned fuel have finite values, there must be a delay in the response of S_T to the changes in the flame configuration, represented by its surface area. Therefore, the degree of correlation between S_T and $A(Y)$ must be a function of a time lag, Δt , between these two quantities. For each value of Y in Fig. 5, we determined the time lag, Δt_c , that produced the best correlation. This was done by directly calculating the cross-correlation between $S_T(t)/S_L$ and $A(Y, t)/L^2$ and finding its maximum. The value obtained for Δt_c was verified by determining the least squares fit for the distribution of $S_T(t)/S_L$ vs. $A(Y, t - \Delta t_c)/L^2$ and by finding $\Delta t'_c$ that maximized the slope of the fit and minimized its residuals. The values of $A(Y)/L^2$ in Fig. 5 were then shifted in time with respect to S_T/S_L by the corresponding time lag Δt_c given in the lower right corner of the panels (a), (c), and (d).

The first key conclusion emerging from Fig. 5 is that S_T and A become progressively less correlated with increasing values of Y . While the correlation is pronounced throughout the reaction zone and is exceptionally strong near the peak reaction rate, S_T and A are only very weakly correlated in the colder parts of the preheat zone. Note that panels (b), (d), and (f) have the same scale, which shows the relative increase in the scatter of the distribution and its overall shift to higher values of A in the preheat zone.

Note in Fig. 5b that at the peak reaction rate, the scatter of the distribution is the largest near the average values of S_T and $A_{0.15}$. At extreme values, however, the scatter becomes very small with data points located very close to the fit line. This effect is much less pronounced for $Y = 0.5$, and for $Y = 0.95$ the scatter appears to increase substantially toward extreme values of $A_{0.95}$.

The time delays that give the best correlation between the two quantities are positive, and thus they show that S_T does indeed lag behind A . Moreover, the magnitude of Δt_c increases with increasing Y . Qualitatively, this agrees with the fact that S_T at a given moment is primarily determined by the region of the highest reaction rate, which corresponds to the lowest values of Y . Consequently, the time delay between S_T and the area of the isosurface representing the peak reaction rate is very small, namely $0.04\tau_{ed}$. Since turbulence reorganizes the flame on a timescale $\sim \tau_{ed}$, such a small lag is too short for the flame structure to change in any significant way. Therefore, the correlation between $A_{0.15}$ and S_T is very strong.

²Note that using instead the expression $\bar{I}(Y) = (\overline{S_T/S_L})/(\overline{A_T(Y)}/L^2)$ gives virtually the same result.

At the same time, since the reaction rate is fairly low at $Y = 0.5$, the contribution of this region to the overall turbulent flame speed is small. Burning still needs to accelerate substantially in this area in order for it to become the new region of peak reaction rate, which will then predominantly determine the magnitude of S_T . The time required for this to occur results in a longer time delay, namely $0.1\tau_{ed}$. During this time, however, turbulence is able to change the flame structure more strongly than in the case of $Y = 0.15$. As a result, the degree of correlation between $A_{0.5}$ and S_T decreases.

In the coldest regions of the preheat zone, there is no correlation between S_T and $A_{0.95}$ at small values of Δt_c . We found evidence of weak correlation for a much larger time delay $\Delta t_c = 0.58\tau_{ed}$. This value, however, is comparable to the time during which the turbulence completely reorganizes the structure of the turbulent flame. Therefore, by the time burning reaches the reactants in the outer regions of the preheat zone, the connection between their original distribution and the resulting turbulent flame speed is significantly disrupted.

We also found weak correlation between $A_{0.95}$ and $A_{0.15}$ with the time lag for $A_{0.95}$ similar to that in the case of S_T , namely $\Delta t_c = 0.56\tau_{ed}$, and the slope of the least squares fit of 0.4907. This weak correlation between $A_{0.15}$ and $A_{0.95}$ is in agreement with a similarly weak correlation between S_T and $A_{0.95}$. In particular, it reflects the fact that after the time $\approx 0.56 - 0.58\tau_{ed}$, burning reaches the outer part of the preheat zone. As a result, the former $Y = 0.95$ region becomes the new $Y = 0.15$ region and thus the new site of the peak reaction rate which now determines S_T . Substantial change in the flame-brush structure during this time, however, leads only to weak correlation between $A_{0.15}$ and $A_{0.95}$.

The computed time delays can be compared with the characteristic propagation time of the laminar flame,

$$\tau_\delta = \frac{\delta_L}{S_L} = \frac{30 L}{8 U} = 3.75\tau_{ed}, \quad (13)$$

and with the adiabatic induction time for the reaction model used in this work,

$$\tau_{ind} = \left(\frac{C_p T}{Bq\rho Y} \right) \left(\frac{RT}{Q} \right) \exp\left(\frac{Q}{RT} \right), \quad (14)$$

where τ_{ind} is based on the Frank-Kamenetskii approximation [23]. In eq. (13), we used the values of L and U given in Table 2.

Eq. (14) is derived under the assumption that heating of a fluid element by chemical energy release greatly exceeds its cooling due to thermal conduction. Therefore, eq. (14) applies only in the reaction zone. There τ_{ind} is the controlling timescale and it is 1 – 2 orders of magnitude smaller than τ_δ . For a planar laminar flame,

$$\begin{aligned} \tau_{ind} &\approx 0.01\tau_\delta \approx 0.05\tau_{ed}, & \text{for } Y = 0.15, \\ \tau_{ind} &\approx 0.06\tau_\delta \approx 0.21\tau_{ed}, & \text{for } Y = 0.5. \end{aligned} \quad (15)$$

This shows that for $Y = 0.15$, τ_{ind} is practically equal to the corresponding time lag, while for $Y = 0.5$, τ_{ind} is within a factor of ≈ 2 of Δt_c (Fig. 5a,c). Using in eq. (14) the specific heat at constant volume, $C_v = R/M(\gamma - 1)$, instead of C_p , i.e., assuming that burning occurs at constant volume rather than at constant pressure, would decrease the values of τ_{ind} by $\approx 15\%$ to $0.04\tau_{ed}$ and $0.18\tau_{ed}$, respectively.

In the preheat zone, τ_{ind} rapidly becomes much larger than τ_δ , since heating and ignition of the reactants now are controlled by heat transfer and the propagation of the flame as a whole. For $Y = 0.95$, however, the time delay $\Delta t_c = 0.58\tau_{ed} \approx 0.16\tau_\delta$. Furthermore, it is an order of magnitude smaller than the time $\tau \approx 1.67\delta_L/S_L = 1.67\tau_\delta$, which is necessary for the flame to propagate over the characteristic distance separating $Y = 0.95$ and $Y = 0.15$ in the flamelet structure (cf. Fig. 7 in [9]). This shows that while in the reaction zone the time delays are in good agreement with the corresponding τ_{ind} , in the preheat zone Δt_c is substantially smaller than the characteristic propagation times of the laminar flame.

In addition to the strong correlation between the values of S_T and $A_{0.15}$, the distribution shown in Fig. 5b has another important property that is not present at higher values of Y . As the flame becomes less convoluted, it will behave progressively more like a planar laminar flame. This means that A_Y/L^2 for the isosurface most representative of the flame surface and S_T/S_L must approach unity simultaneously. Consider now the linear least squares fit for the case $Y = 0.15$, shown with a solid line in Fig. 5b. It has the form

$$\frac{S_T}{S_L} = 1.44 \frac{A_{0.15}}{L^2} - 0.41. \quad (16)$$

For $A_{0.15}/L^2 = 1$, this expression gives $S_T/S_L = 1.03$, which is the deviation of only 3% from unity. In fact, the line which passes exactly through the point $S_T/S_L = A_{0.15}/L^2 = 1$ and also, as required for the least squares fit, through

the center of mass of the distribution, i.e., the point $S_T/S_L = \bar{S}_T/S_L$ and $A_{0.15}/L^2 = \bar{A}_{0.15}/L^2$, is

$$\frac{S_T}{S_L} = \left\{ \frac{(\bar{S}_T/S_L) - 1}{(\bar{A}_{0.15}/L^2) - 1} \right\} \frac{A_{0.15}}{L^2} - \left\{ \frac{(\bar{S}_T/S_L) - (\bar{A}_{0.15}/L^2)}{(\bar{A}_{0.15}/L^2) - 1} \right\} = 1.46 \frac{A_{0.15}}{L^2} - 0.46. \quad (17)$$

Here \bar{S}_T/S_L and $\bar{A}_{0.15}/L^2$ are the time-averaged values given in Table 3. Expressions for the coefficients in eq. (17) approximate the first and second coefficients in eq. (16) with the accuracy of $\approx 1\%$ and $\approx 12\%$, respectively.

This demonstrates that the distribution of S_T/S_L as a function of $A_{0.15}/L^2$ (Fig. 5b) closely follows the trend that has the correct limiting behavior as $A_{0.15}/L^2 \rightarrow 1$. Linear least squares fits for the two other values of Y , shown in Fig. 5d,f, do not recover the value of $S_T/S_L = 1$ as $A(Y)/L^2 \rightarrow 1$. It is particularly important to consider such limiting behavior for $Y = 0.5$, where a reasonably good correlation between S_T and $A_{0.5}$ could suggest that this value of Y can also be viewed as representative of the flame properties.

Next consider the correlation of $A(Y)$ with the second key global characteristic of the turbulent flame, namely its width, δ_T . Fig. 6 shows the correlation between $A(Y)/L^2$ and δ_T/L for the same three values of Y as in Fig. 5. Since both A and δ_T represent the same instantaneous configuration of the flame, no time delay between them would be expected.³ Consequently, no time shift was applied to either quantity in Fig. 6.

The distribution of δ_T/L as a function of $A(Y)/L^2$ shows the same trend observed for S_T/S_L . In particular, the correlation between the two quantities is also the strongest for $Y = 0.15$, and it decreases with increasing Y . The values of δ_T/L and $A_{0.95}$ appear to be almost completely uncorrelated. Note, however, that overall the correlation in the reaction zone, and, in particular, in the region of peak reaction rate, is weaker for δ_T than S_T with the distributions of δ_T having a much larger scatter.

The decrease in correlation between δ_T/L and $A(Y)/L^2$ with increasing Y reflects the fact that the isosurfaces of higher Y tend to be wrinkled on progressively smaller scales, as discussed in § 3.1 (also see [9]). As a result, while the areas of these isosurfaces increase, they contribute less to δ_T which is determined predominantly by the flame folding on the largest scales. Therefore, δ_T is best correlated with $A(Y)$ at the lowest values of Y , where the folding on such large scales is most pronounced.

The strong correlation of $A_{0.15}$ with S_T and δ_T , which represent both the global energetics and the global structure of the turbulent flame, as well as the correct limiting behavior of the distribution of S_T/S_L as $A_{0.15}/L^2 \rightarrow 1$ present a compelling case. These results show that $Y = 0.15$ most accurately characterizes the overall evolution of the flame. Consequently, the flame surface area, A_T , is best represented by the isosurfaces of Y close to the peak reaction rate.

3.4. Stretch factor and the balance between S_T and A_T

We can now revisit the question of the actual values of the stretch factor, I , in the regime considered here.⁴ Our results demonstrate that $I_{0.15}$ must be viewed as most characteristic of the system evolution. The time history of $I_{0.15}$ (Fig. 4a) and its time-averaged values (Table 3) show pronounced deviation from Damköhler's concept on the order of 30% as the turbulent flame speed exhibits a strong exaggerated response to the increase in the flame surface area.

This exaggerated response is illustrated in Fig. 5 as the shaded gray area. In particular, the shaded region in Fig. 5b is a measure of the relative increase of the actual values of S_T/S_L with respect to the values given by $A_{0.15}/L^2$, which are shown as a dash-dot line. At larger values of $A_{0.15}/L^2$, the overall distribution deviates progressively more from the $S_T/S_L = A_{0.15}/L^2$ line. This demonstrates the following crucial fact: the magnitude of the exaggerated response of S_T grows with increasing flame surface area. We examine this result in more detail in § 4.3.

Finally, the time-averaged value of the stretch factor $\bar{I} \approx 1$ in the coldest region of the preheat zone (Fig. 4b) was, in fact, simply the result of time averaging. Fig. 5e,f shows that $I_{0.95}$ has a much larger range of variability than $I_{0.15}$, namely $0.5 - 1.7$ (also consider the $\pm\sigma$ standard deviation of $I(Y)$ shown in Fig. 4b). At the same time, in a system in which S_T is determined only by A_T , I by definition must be unity and constant. This further shows that $\bar{I} \approx 1$ at large values of Y in simulation S3 cannot serve as evidence of the fact that the observed S_T is determined only by the increase in the flame surface area.

³As a check, we verified that, indeed, the cross-correlation had its maximum at the zero time lag.

⁴In light of the fact that S_T and $A(Y)$ are best correlated when A is shifted in time with respect to S_T , the question arises whether such time shift should also be applied to A when calculating I , i.e., whether the expression $I(Y, t) = (S_T(t)/S_L)/(A(Y, t - \Delta t_c)/L^2)$ should be used. In principle, an argument could be made that, due to the inherent delay in the response of S_T to the changes in the flame structure, the current value of S_T is the result of A that existed earlier in time and, thus, I must be calculated using this earlier value. At the same time, as was shown, the time lag Δt_c is extremely small for $Y = 0.15$, which as we have concluded should be used to estimate I . During this time, the change in the flame surface area is negligible and applying the time shift in the expression for I does not cause any appreciable change in the result.

4. Flame surface density and its relation to the turbulent flame speed

4.1. Surface density of the fuel mass fraction isosurfaces

The analysis of the flame surface area does not address the question of how the flamelets are organized inside the flame brush and, in particular, how tightly they are packed. It can be seen in Fig. 6b that the relative variation of $A_{0.15}$ is $\approx 50\%$ larger than that of δ_T with the ratio of the maximum and minimum values of $A_{0.15}$ being ≈ 3 as opposed to ≈ 2 for δ_T . This suggests that the change in the flame surface area cannot be accounted for only by the variations in the turbulent flame thickness, but it must also be related to how the flame surface is folded inside the flame brush.

Consider the surface density of the fuel mass fraction isosurfaces, defined as the isosurface area normalized by the effective flame-brush volume

$$\Sigma(Y) = \frac{A(Y)}{\delta_T L^2}. \quad (18)$$

Detailed discussion of this definition of $\Sigma(Y)$ and, in particular, of the choice of the uniform normalization by the full flame-brush volume is given in Appendix A.

The evolution of $\Sigma_{0.01}$ and $\Sigma_{0.99}$, where $\Sigma_{Y'} \equiv \Sigma(Y = Y')$, is shown in Fig. 7a,b. The overall trends are similar to those exhibited by $A_{0.01}$ and $A_{0.99}$ (cf. Fig. 3a,b). In particular, Σ is lower on the product side of the flame. Moreover, similar to A , Σ appears to converge at lower values of Y and shows virtually no convergence in the preheat zone. Most important, there is substantial variability in Σ , especially on the fuel side, where Σ changes by up to a factor of 3. This tighter packing of the isosurfaces, which periodically occurs in the course of system evolution, suggests that the increase in the flame surface area is indeed associated with the increase not only of δ_T , but also of Σ .

Fig. 7c shows time-averaged distributions of $\Sigma(Y)$ in simulations S1 - S3. Comparison with Fig. 3c demonstrates that both $\bar{A}(Y)/L^2$ and $\bar{\Sigma}(Y)$ show remarkably similar behavior. The time-averaged values of $\bar{\Sigma}$ are also not constant, but, instead, they progressively increase through the flamelet from its product side to the fuel side. The resulting inverted-S shape of the profiles is very similar to that of $\bar{A}(Y)$ with both \bar{A} and $\bar{\Sigma}$ at the two extreme values of Y ($Y = 0.01$ and 0.99) differing in S3 by almost a factor of two. Similar to \bar{A} , $\bar{\Sigma}$ varies the least in the interior of the reaction zone, i.e., for $Y \approx 0.15 - 0.6$, while outside this region it shows strong dependence on Y . Just outside the reaction zone, individual profiles begin to diverge from each other with the variation between them becoming progressively larger for higher values of Y .

In the reaction zone, values of $\bar{\Sigma}$ for all three calculations are much closer than those of \bar{A} . In fact, Table 3 shows that $\bar{\Sigma}(Y)$ exhibits 4th-order convergence compared with 3rd-order convergence for \bar{A} . As a result, values of $\bar{\Sigma}$ are virtually identical for $Y \approx 0.01 - 0.4$ in S2 and S3. On the other hand, in the preheat zone, the profiles of $\bar{\Sigma}$ diverge more than in the case of \bar{A} . This shows that the effects of small-scale turbulent motions on the reaction and the preheat zones are, in fact, even more disparate in terms of their ability to provide tight folding of the isosurfaces compared with their ability to increase the isosurface area.

Flame surface density is a quantity used both in experimental and theoretical combustion research. In particular, Σ_{max} is defined as the surface density in the region of the flame brush with mean reactedness $\bar{c} = 0.5$, where $c = (T - T_0)/(T_P - T_0)$. It can then be shown that [3]

$$\Sigma_{max} = \frac{A_{0.5}^*}{\delta_T A_L^*}, \quad (19)$$

where $A_{0.5}^*$ is the flamelet surface area based on $\bar{c} = 0.5$, and A_L^* represents the average area of the flame brush. In a system described by the one-step Arrhenius kinetics, $\bar{c} = 0.5$ corresponds to $Y = 0.5$. Therefore, $A_{0.5}^* \equiv A_{0.5}$. At the same time, in a planar brush $A_L^* = L^2$, as was discussed in § 3.1. Thus, Σ_{max} is equivalent to $\Sigma_{0.5}$ as given by eq. (18). It is reasonable then to compare values of $\Sigma_{0.5}$ in our simulations with those of Σ_{max} obtained in other experimental and numerical settings. In particular, in S3, $\bar{\Sigma}_{0.5} = 0.73 \text{ mm}^{-1}$. This is comparable to the range of values of $\Sigma_{max} \approx 0.12 - 0.6 \text{ mm}^{-1}$ obtained in a number of experimental studies using a wide variety of flame configurations (see [3] for a summary table). The fact that the value in S3 is somewhat larger is not surprising, given that the turbulent intensity in it is substantially higher.

Overall, however, the traditional definition of Σ given in [3] is not equivalent to the definition used here unless $Y = 0.5$. Therefore, unlike Σ_{max} , $\Sigma_{0.5}$ is not necessarily the maximum value of Σ for all values of Y . Fig. 7c shows that while in S1 $\bar{\Sigma}_{0.5}$ is indeed approximately the largest value, this is not the case in S2 and S3. At the same time, in all three calculations, $\bar{\Sigma}_{0.5}$ is representative of the values of $\bar{\Sigma}$ throughout the reaction zone with the difference between $\bar{\Sigma}_{0.5}$ and $\bar{\Sigma}_{0.15}$ being $\approx 6-9\%$ in the higher-resolution cases.

4.2. Distributions of $\bar{A}(Y)$ and $\bar{\Sigma}(Y)$ and the effects of small-scale turbulence

How do these results concerning the distributions of $A(Y)$ and $\Sigma(Y)$ relate to previous conclusions [9] regarding the inability of the turbulent cascade to penetrate the flamelet interior and the role of small-scale turbulent motions? As

was discussed in § 2.1 (also see [9] for further details), the progressive increase in resolution from S1 to S3 extends the turbulent cascade to smaller scales, and this leads to a substantial increase in the energy of turbulent motions on scales $\lambda \lesssim \delta_L$ in nonreactive turbulence. This increase in resolution was found to cause the flame surface on the fuel side to be wrinkled on progressively finer scales, while remaining virtually unchanged on the product side. It was determined that the deviation of the internal flamelet structure from that of the planar laminar flame increases with decreasing temperature. These two results showed that the effects of small-scale turbulent motions are most pronounced in the coldest parts of the preheat zone. These effects diminish with increasing temperature and completely disappear once the reaction rate becomes significant [9].

Results presented in this paper are consistent with this picture. The steady growth of \bar{A}/L^2 and $\bar{\Sigma}$ on the fuel side of the preheat zone with increasing resolution shows that more intense small-scale motions indeed fold isosurfaces on progressively finer scales. It must be emphasized that the change in A alone does not necessarily mean that it is caused by finer wrinkling on smaller scales. Only when viewed in conjunction with the surface density, which shows a very similar dependence on Y , does such increase in A serve as a strong indication of the small-scale wrinkling.

With increasing temperature, not only do \bar{A}/L^2 and $\bar{\Sigma}$ decrease rapidly, but also, most importantly, individual profiles for S2 and S3 begin to approach each other. This demonstrates that the main difference between these two simulations, namely the presence of more energetic small-scale turbulence in S3, is being eliminated and, thereby, motions on scales $\lambda < \delta_L$ are gradually suppressed. Since it is these small scales that enhance the diffusive transport, which in turn broadens the preheat zone, their suppression causes the internal flame structure to approach that of the planar laminar flame [9].

As the reaction rate becomes substantial at $Y \lesssim 0.5$, both \bar{A}/L^2 and $\bar{\Sigma}$ become similar in S2 and S3. At this point the only energetic scales are $\lambda \gtrsim \delta_L$, which are originally the same in both calculations (cf. Fig. 1 in [9]). Consequently, they generate similar isosurface areas and densities. Since these scales cannot support small-scale diffusive transport, any broadening of the internal flamelet structure effectively disappears at $Y \lesssim 0.5$ [9]. Further decrease in \bar{A}/L^2 and $\bar{\Sigma}$ is the consequence of the continued suppression of the progressively larger scales $\lambda > \delta_L$.

There is one important distinction between the distributions of \bar{A}/L^2 and $\bar{\Sigma}$ and the time-averaged profiles of Y and T , which represent the internal flamelet structure [9]. The Y and T profiles showed very little variation between simulations S1-S3 not only in the reaction zone, but also in the preheat zone. This is in contrast with the distributions \bar{A}/L^2 and $\bar{\Sigma}$, which differ substantially in the preheat zone even between the S2 and S3.

This suggests that small scales, $\lambda < \delta_L$, contribute differently to the turbulent diffusive transport and to the wrinkling of the isosurfaces. The former is primarily governed by the largest of these small scales, i.e., scales not much smaller than δ_L , since these scales have the highest velocities associated with them. The energy on these scales is the same in all three simulations and, thus, they produce the same structure of the broadened preheat zone. At the same time, all scales smaller than δ_L contribute to the isosurface wrinkling and the different energy content of these scales causes the distributions of \bar{A}/L^2 and $\bar{\Sigma}$ to differ substantially in the preheat zone.

Qualitatively, both the internal flamelet structure described in [9] and the distributions of A and Σ presented here create a consistent picture of the profound transformation that turbulence undergoes as it passes through the flame. Changes in the energy budget between different scales, which are most certainly accompanied by the development of both anisotropy and inhomogeneity of the velocity field, are complex. While the evidence presented here and in [9] provide hints about the nature of this transformation, the details remain unknown. For instance, are the energy release and the resulting fluid expansion the only effects responsible for altering the turbulent field and redistributing energy between different scales? What are the relative contributions of various small scales to the increase in A and Σ ? How does the shift in balance between small and large scales with increasing temperature change at different turbulent intensities? All of these questions need to be addressed in future studies.

4.3. Correlation between S_T and $\Sigma(Y)$

Peaks and troughs in values of $\Sigma_{0.01}$ in Fig. 7a can generally be associated with those in values of S_T in Fig. 1b. This suggests that the density of the flame surface, packed inside the flame brush, is a dynamically important characteristic affecting the energetics of the system and, thus, its evolution. In order to consider this question more rigorously, we show in Fig. 8 the correlation between S_T/S_L and $\Sigma(Y)$ for the same three values of Y as in Figs. 5-6.

As with A , one would expect S_T to respond with a certain delay to the changes in Σ . Even though both A and Σ represent the same instantaneous flame structure, we chose not to make an *a priori* assumption that the magnitude of that delay is the same as it was in the case of A . We determined the time lag, Δt_c , which produced the best correlation between $S_T(t)/S_L$ and $\Sigma(Y, t)$, for each individual value of Y following the same procedure as was used in § 3.3. The values of $\Sigma(Y)$ in Fig. 8 were shifted in time by Δt_c given in the lower right corner of the panels (a), (c), and (d).

The principal result is the strong correlation of the values of $\Sigma_{0.15}$, corresponding to the region of the peak reaction rate in the flamelet, with S_T . The scatter of the distribution of S_T/S_L as a function of $\Sigma_{0.15}$, however, is larger than for $A_{0.15}$. At $Y = 0.5$, the correlation of S_T with $\Sigma_{0.5}$ is weaker, as for $A_{0.5}$, although it is still quite pronounced. Finally,

similar to $A_{0.95}$, $\Sigma_{0.95}$ shows at most only very weak correlation with S_T at $\Delta t_c = 0.58\tau_{ed}$ (Fig. 8f). In addition, we found some evidence of weak anticorrelation of $\Sigma_{0.95}$ with S_T at $\Delta t_c = 0$, with the slope of the least squares fit of -3.007 . This is in contrast to $A_{0.95}$, which was completely uncorrelated with S_T at values of Δt_c close to zero. It is not clear, however, what the physical significance of this anticorrelation is, since it is unlikely for S_T to have an instantaneous response to the distribution of cold unreacted fuel.⁵

The time delays for Σ in the reaction zone are similar to those obtained in the case of A . Moreover, Δt_c for $\Sigma_{0.5}$ is much closer to the magnitude of the induction time given in eq. (14), than it was for $A_{0.5}$, being within 25% of the corresponding value of τ_{ind} .

These results are further evidence that Y close to the peak reaction rate is most representative of the dynamics of the turbulent flame. Therefore, as $A_{0.15}$ was concluded in § 3.3 to represent the flame surface area, $\Sigma_{0.15}$ can be viewed to represent the flame surface density, Σ_T . Consequently, the fact that larger values of S_T are correlated with larger values of $\Sigma_{0.15}$ shows that the increase of S_T is closely associated with more tightly packed flame configurations.

So far we have considered the correlation between S_T , $A_{0.15}$, and $\Sigma_{0.15}$ separately. In order to demonstrate the close connection between these three quantities, we colored each data point in Fig. 3b according to the corresponding magnitude of $\Sigma_{0.15}$. It can be seen that, indeed, larger values of S_T and $A_{0.15}$ are associated with larger values of $\Sigma_{0.15}$. In particular, an increase in the value of $I_{0.15}$ from ≈ 1.2 to ≈ 1.36 is associated with the increase in $\Sigma_{0.15}$ by more than a factor of two from $\approx 0.4 \text{ mm}^{-1}$ to $\approx 0.85 \text{ mm}^{-1}$.

This finally leads us to the following two key conclusions:

1. Larger values of A_T are associated with larger values of Σ_T . This shows that increase in the flame surface area in the course of the flame evolution is primarily due to the much tighter folding and packing of the flame, rather than only due to the increase in the overall extent of the flame brush.
2. Increase in A_T and Σ_T leads not only to larger values of S_T but, most importantly, also to a larger deviation of S_T/S_L from A_T/L^2 , i.e., from the value predicted by Damköhler's concept. In other words, in the presence of the high-speed turbulence, the increase in the flame surface area and the associated tighter packing of the flame result in the progressively more exaggerated response of S_T to such increase in A_T . This, therefore, causes a substantially accelerated burning.

5. Mechanism of the turbulent flame speed increase

5.1. Potential causes of the increase of the local burning speed

The substantial deviation of I from unity observed in the simulations brings up the following question: What mechanism is responsible for raising S_T beyond what can be attributed to the increase in A_T ?

According to Damköhler's concept, $I > 1$ results from the change in the local flame speed, S_l , which is the consequence of the enhancement of diffusive processes by turbulent transport. Therefore, this change cannot be episodic and local, but rather it must be a reflection of the statistically dominant state. It was demonstrated in [9], however, that there is no evidence of such enhancement, as the average internal flamelet structure in the reaction zone is virtually identical to that of the planar laminar flame, and the resulting thermal width of the flamelets is practically equal to δ_L . Since for the first-order Arrhenius kinetics there is a unique correspondence between the flame structure and speed, this showed that, on average, the flame propagates locally with the speed close to S_L . Furthermore, there is no significant fuel preconditioning by the turbulent flow, which could increase S_l . For the full duration of the simulations, the pressure in the domain remains smooth and close to its initial value P_0 . The fuel temperature rises by the end of the simulation to $\approx 330K$, which is not sufficient to increase S_l appreciably.

These considerations show that the observed anomalous increase in S_T cannot be accommodated within Damköhler's paradigm. Consequently, a different mechanism must augment the effect of the increased flame surface area.

Instead of being the result of a uniform global increase of S_l compared to S_L throughout the flame brush, enhanced values of S_T could be caused by a significant local increase in S_l . Two immediate causes for such local enhancement can be envisaged: (1) local inhomogeneities in the thermodynamic state of the fuel, and (2) intermittency of the turbulent flow.

We did not find, however, either of them to be a significant factor in causing the observed increase in S_T . In particular, in a subsonic turbulent flow, such as the one considered here, with the turbulent Mach number Ma substantially less than unity (see Table 1), local variations of density or temperature are much too small to affect S_l in any appreciable way.

⁵We note that we were unable to find any statistically significant correlation or anticorrelation between $\Sigma_{0.15}$ and $\Sigma_{0.95}$ at any time lag. This is in contrast with the weak correlation between $A_{0.15}$ and $A_{0.95}$ discussed in § 3.3.

The potential role of turbulence intermittency on the flame has been studied by Pan et al. [24] in the context of the Rayleigh-Taylor-driven thermonuclear flames in the interior of a white dwarf during the Type Ia supernova explosion. Their results suggested the possibility that intermittency in the velocity field causes local disruption and broadening of the flame, which potentially would also increase the local burning speed. It is not immediately clear, however, to what degree their conclusions would apply to the system discussed here. The conditions in the white dwarf interior considered in [24] are substantially different from the ones in S1 - S3. Moreover, their analysis did not consider any feedback of the flame on the turbulent field and, in particular, it did not include fluid expansion due to heat release which invariably affects intermittency of the flow. While we do observe intermittency in the flow field in our simulations, we find that regions of large velocity enhancement are statistically too rare, their spatial extent is too small, and they are much too short lived to increase S_l and, thus, to make any significant contribution to the overall increase in S_T . At the same time, the role of intermittency in the dynamics of turbulent flames does require further investigation. In particular, it would be extremely important to extend the analysis of Pan et al. [24] by including the feedback of the flame on turbulence under conditions characteristic of chemical rather than thermonuclear flames.

5.2. Local increase of S_l in cusps formed by flame collisions

According to the theory of flame stretch (see [5] for a review), under the $Le = 1$ conditions, the flame is not affected either by the flow-induced strain or curvature, in accordance with Damköhler's concept. In particular, a stationary spherical flame supported by a point source of mass, which is an example of a curved unstrained flame, has the internal structure, and thus local burning velocity, identical to that of a planar laminar flame [5]. Such analysis, however, is typically performed in the regime when curvature radius $r_c \gg \delta_L$. Our simulations of an idealized spherical or cylindrical flame collapsing into a stationary fuel corroborate this result. Furthermore, they show that $S_l = S_L$ not only when $r_c \gg \delta_L$, but up until the moment when the flame curvature becomes $\approx 1/\delta_L$, i.e., until the flame effectively collapses onto itself. At this point, S_l increases substantially. Beyond this moment, however, the flame itself effectively ceases to exist and, therefore, the local flame speed loses its meaning. Such idealized situation is hardly representative of the conditions arising in an actual turbulent flame. Nonetheless, regions of large flame curvature $\sim 1/\delta_L$ are frequently created in the high-speed turbulent flow considered here, and we now show how they naturally provide a mechanism for a significant local enhancement of S_l .

We have demonstrated above that in the presence of intense turbulence, larger values of I are well correlated with the increase in Σ and, thus, with much tighter folding and packing of the flamelets inside the flame brush. The inverse of the surface density is a measure of an average separation between surface elements. Given that $\bar{\Sigma}_{0.15} = 0.67 \text{ mm}^{-1}$ in simulation S3, the average distance between individual flame sheets is $1/\bar{\Sigma}_{0.15} \approx 1.49 \text{ mm} \approx 4.7\delta_L$. At the same time, $\Sigma_{0.15}$ can be as high as 0.97 mm^{-1} (Figs. 5b, 8b), resulting in an even lower average separation of $\approx 3.2\delta_L$. This is comparable to the full width of individual flamelets (cf. Fig. 7 in [9]). Such tightly folded flamelet configurations invariably result in frequent collisions of individual flame sheets.

Fig. 9 gives an example of such collision in simulation S3. The figure shows the flame-brush structure at three times: $11.86\tau_{ed}$ (upper panel), as well as $0.1\tau_{ed} = 3 \mu\text{s}$ and $0.2\tau_{ed} = 6 \mu\text{s}$ later (middle and lower panels, respectively). Initially, a region with highly convolved flame develops in the flame brush (region A). At this time, $S_l = S_L$ locally throughout region A and self-propagation of the flame can be neglected on timescales considered in Fig. 9. As turbulent motions continue to bring individual flame sheets closer to each other, the curvature radius of the flame becomes close to δ_L , and the preheat zones begin to overlap substantially over an extended region of the flame surface. This marks the formation of two regions of high flame curvature $\gtrsim 1/\delta_L$ (regions B), which we will hereafter refer to as "cusps." Regions C in the lower panel show that $3 \mu\text{s}$ later the flame sheets have merged and formed two extended reaction zones, which suggests substantially accelerated burning in that area of the flame brush. Note also a rapid decrease of the area of the $Y = 0.5$ isosurface represented with the thin black line. Comparison of regions B and C shows that this isosurface propagated over the distance $\approx 0.5 \text{ mm}$ over the time $3 \mu\text{s}$, which implies the propagation speed (but not the local burning speed) $\approx 55S_L$. During the time shown in Fig. 9, two other highly elongated regions of flame collision have formed near the upper face of the domain. Thus, Fig. 9 illustrates the fact that flame collisions are ubiquitous in the turbulent flame, and they do produce regions of large flame curvature. Moreover, their evolution in Fig. 9 suggests substantial increase of both the local burning and propagation speeds in the cusps.

5.3. Structure and properties of cusps

Cusps were first considered by Zel'dovich [25] (also see [26]), who suggested them as a mechanism of flame stabilization that prevents the unbounded exponential growth of the flame surface under the action of the Landau-Darrieus instability [27]. Such regions would have a high propagation velocity, causing rapid annealing of the flame surface, and thus providing an efficient mechanism to counterbalance the flame instability [25]. It was also suggested in [25] that S_l near the tip of the cusp ceases to be equal to S_L , and the cusp region develops a structure similar to the tip of the Bunsen flame. The flame in the analysis given in [25, 26], however, was considered to be a gasdynamic

discontinuity, and so its internal structure was ignored. As a result, the actual increase of the local flame speed in the cusp could not be determined.

In order to analyze quantitatively the effect of flame collisions and to determine the actual increase of S_l in the resulting cusps, consider an idealized model of the cusps observed in Fig. 9. In particular, consider two symmetrically located planar flame sheets approaching each other with the inclination angle to the mid-plane α . At the point of collision, the flame sheets merge and form a cusp. Its properties, such as its structure, speed of propagation, and effective burning velocity, are determined in this configuration only by two parameters, S_L and α .

Fig. 10 illustrates the flame structure formed in this situation. It shows the distribution of the fuel mass fraction in two simulations performed for $\alpha = 1^\circ$ and $\alpha = 4^\circ$ with Athena-RFX using the same physical model as in simulations S1 - S3. The domain has the resolution $\Delta x = \delta_L/32$ and zero-order extrapolation boundary conditions on all sides. At $t = 0$, two intersecting flame sheets were initialized with the exact structure of the planar laminar flame, and uniform pressure P_0 and zero velocities were assumed. After the initial transient stage, the flame develops the structure shown in Fig. 10. The structure of the cusp itself does not change with time, provided that the planar flame sheets extend sufficiently far from it. Therefore, Fig. 10 can be viewed as a steady-state solution.

Fig. 10 shows that flame collision at very low inclination angles results in the formation of a highly elongated structure. It is formed by rapid heating and, subsequently, ignition of a larger amount of fuel than in the planar laminar flame due to the focusing of the thermal flux from two approaching flame sheets. Consequently, its extent is determined by the size of the region in which the preheat zones of approaching flames overlap and, thus, create the necessary enhanced thermal flux. Since the width of the preheat zone is $\approx \delta_L$, very small values of α are required for the cusp to be substantially broader than δ_L . This can further be seen in the distributions of the fuel mass fraction, Y , temperature, T , and reaction rate, \dot{Y} , along the symmetry axis of the cusp shown in Fig. 11. The structure of the reaction zone in the cusp very quickly approaches that of the laminar flame with two becoming very close to each other already at $\alpha \sim 4^\circ$. At the same time, the preheat zone of the cusp remains substantially broadened for much larger values of α .

There are three characteristic speeds in this problem. Sufficiently far from the tip of the cusp, the flame locally propagates normal to its surface with the laminar flame speed S_L , i.e., there $S_l = S_L$. The cusp itself moves into the fuel with the phase velocity D_c , which results simply from the two inclined planar surfaces colliding with each other. This speed can be determined based on purely geometrical considerations [25],

$$D_c = \frac{S_L}{\sin \alpha}. \quad (20)$$

This cusp propagation speed, normalized by S_L , is shown as a solid line in Fig. 12a along with D_c/S_L determined as the velocity of the leftmost point of the $Y = 0.5$ isosurface in simulations for four values of α . Eq. (20) is within $\lesssim 1\%$ accuracy of the computed values. D_c approaches the laminar flame speed as $\alpha \rightarrow 90^\circ$, i.e., when the two flame sheets cease to advance toward each other. At the opposite limit of small α , D_c can be quite large and, in principle, infinite when $\alpha \rightarrow 0^\circ$. In particular, at $\alpha \approx 0.5^\circ$, D_c becomes larger than the sound speed in cold fuel indicated with the horizontal dashed line in Fig. 12a. Note also that at $\alpha = 1^\circ$, the value of $D_c \approx 57S_L$ is very close to the high propagation velocity $\approx 55S_L$ of cusps in regions B - C in Fig. 9 estimated in § 5.2.

The third characteristic speed, which is of most importance to us, is the local burning speed in the cusp, S_l . The broadened reaction zone at low flame-inclination angles (Figs. 10 and 11b) causes more fuel to be consumed per unit flame surface area than in the planar laminar flame, and, therefore, it leads to a larger local flame speed $S_l > S_L$. Since the reaction zone width is the largest at the tip of the cusp, S_l has its maximum there and it gradually decreases to its laminar value S_L in the planar regions of the flame sufficiently far from the cusp. The maximum value of S_l at the cusp tip can be found as

$$S_l^* \equiv \max(S_l) = \frac{1}{\rho_0} \int \rho \dot{Y} dx = -\frac{B}{\rho_0} \int \rho^2 Y \exp\left(-\frac{Q}{RT}\right) dx. \quad (21)$$

Here eq. (7) was used for \dot{Y} , and the integral is taken along the symmetry axis of the cusp shown in Fig. 10. Fig. 12b shows the computed values of S_l^* normalized by S_L for the same four inclination angles as in Fig. 12a.

Two key conclusions emerge from Fig. 12. First, S_l^* is substantially lower than D_c , being less by more than an order of magnitude at the values of α considered. Second and most important, S_l^* can indeed be substantially higher than S_L at small inclination angles.

5.4. Connection between the increase of S_l in cusps and S_T

We are interested, however, not just in S_l but, rather, in the burning speed of an extended flame region, as this is a direct equivalent of the turbulent flame speed. The total burning speed of the flame configuration shown in Fig. 10 is

$$S_c = \frac{\dot{m}_R}{\rho_0}, \quad (22)$$

where \dot{m}_R is the total mass of reactants converted into product per unit time. If the flame were to propagate everywhere with the speed S_L , then $S_c = AS_L$, where A is the surface area of the flame in such a configuration based on the isosurface of $Y = 0.15$ representing the peak reaction rate. Otherwise,

$$I = \frac{S_c}{AS_L} > 1. \quad (23)$$

Here I again is the stretch factor, which is equivalent to the definition used in eq. (12) in the context of the turbulent flame speed. Substituting the definition of S_T given by eq. (10) into the definition of I given by eq. (12), it can be seen that indeed $\dot{m}_R/\rho_0 = IAS_L = S_c$.

Since S_l monotonically decreases away from the cusp, both S_c and I depend on the size of the flame region being considered. This size can be represented by the length l_c , illustrated in Fig. 10, which is defined as the distance from the leftmost point of the isosurface of $Y = 0.15$ in the direction of cusp propagation. Considering different values of l_c is equivalent to varying the fraction of the total surface area of the flame in Fig. 10 represented by the planar section in which $S_l \approx S_L$. Consequently, this allows one to vary the relative contribution to S_c , and thus to I , of the cusp in which $S_l > S_L$.

The stretch factor, calculated using eqs. (22)-(23), is shown in Fig. 13b for four values of α as a function of l_c/δ_L . At smaller l_c close to the width of the reaction zone for a given α (Fig. 11b), I essentially reflects only the values of S_l in the immediate vicinity of the tip of the cusp. On the other hand, at larger l_c , the surface area of the planar flame region, in which $S_l \approx S_L$, is larger and, thus, such region represents a greater fraction of the total surface area of the flame configuration shown in Fig. 10. As a result, the contribution of the planar flame starts to dominate that of the cusp, which causes $I \rightarrow 1$ as seen in Fig. 13b. At lower inclination angles, however, the region in which $S_l > S_L$ extends progressively further from the cusp tip. In particular, at $\alpha = 1^\circ$, I is substantially greater than unity even at $l_c \gg \delta_L$. At the same time, already at $\alpha = 4^\circ$, I drops to $\lesssim 1.04$ at $l_c \approx 5\delta_L$ which shows that S_l recovers its laminar value within a few laminar flame widths from the cusp tip.

These results show that the formation of a cusp due to the collision of planar flame sheets indeed produces values of I substantially larger than unity and comparable to those observed in the simulations presented here. As a result of a higher local flame speed in a cusp, its contribution to the global turbulent burning speed is disproportionately large compared to the fraction of the instantaneous flame surface area in it. A more complex flame configuration, consisting of multiple planar flame sheets that approach each other and collide forming multiple cusps, can then be viewed as a simple model of the turbulent flame. If the flame surface density in this system is increased, flame sheets will get closer to each other causing flame collisions to become more frequent and the resulting cusps to become more numerous. Consequently, the fraction of the flame surface area contained in cusps will increase and I will grow rapidly and significantly, which is demonstrated by the increase in I with decreasing l_c .

This simplified model does not take into account the full complexity of an actual turbulent flame. Such flame does not consist of perfectly planar flame sheets that merge, but instead it is constantly wrinkled and folded on a variety of scales. The analysis presented in § 5.3 shows that in a curved flame, S_l , unlike D_c , does not gradually rise with increasing curvature. Instead, S_l remains very close to its laminar value until the curvature becomes very large, i.e., $\gtrsim 1/\delta_L$, which is consistent with the behavior of an ideal collapsing spherical or cylindrical flame discussed in § 5.2. Turbulence can create regions of such large curvature either by folding the flame, thereby, gradually increasing the curvature at a specific point of the flame surface until it becomes $\gtrsim 1/\delta_L$, or by bringing two flame sheets together until they merge. Both of these situations, however, are, in fact, flame collisions. When they occur, the cusp forms and only then the local flame speed in it increases.

Based on these considerations, the following picture emerges. At low turbulent intensities, the flame surface is wrinkled (or folded) primarily on larger scales with the curvature radius at each point $\gg \delta_L$. Consequently, the flame propagates locally with its laminar speed, and the total $S_T \propto A_T$. Individual cusps can form even at low turbulent intensities as a result of the collision of individual flame sheets. At low values of Σ , however, cusps are infrequent and they represent only a small fraction of the total flame surface resulting in $I \approx 1$. This is analogous to the situation considered above when l_c is large. As the turbulent intensity increases, turbulence is not able to disrupt the internal structure of the flamelets causing flamelets to retain locally their laminar structure and velocity. Instead, turbulent motions are much more efficient at folding the flame with increasingly greater curvature, creating a tightly packed

configuration with large Σ . This increases the frequency of flame collisions and results in a much higher rate of cusp formation. Consequently, a progressively larger fraction of A_T is contained in cusps, which, by analogy with lower values of l_c , leads to $I > 1$.

This picture reconciles the seeming contradiction discussed above between the need for the enhanced local flame speed, as suggested by values of $I > 1$, and the absence of such enhancement globally throughout the flame by the turbulent diffusive transport, as evidenced by the absence of the flame broadening. The flame speed can be significantly enhanced locally in cusps due to thermal flux focusing and not because the flame itself is disrupted and broadened by turbulence.

This simple model of cusp formation demonstrates the mechanism through which S_T can produce an exaggerated response to the increase in A_T . At the same time, in an actual turbulent flame cusps will form in a multitude of configurations. For instance, in addition to the purely two-dimensional situation considered here, there will also be 3D flame collisions which will result in even higher local flame speeds in the cusps and, thus, will have an even larger effect on the magnitude of I . Therefore, in order to predict a particular value of I which can be expected in the turbulent flow of a specific intensity, it is necessary to understand the types of cusps which can form, the local flame speed of each type, its probability of formation, and, thus, the contribution of each type to the exaggerated response of S_T . Such detailed analysis is the subject for future studies.

5.5. Criterion for onset of the cusp-dominated regime of flame evolution

The model of cusp formation can be used to determine the critical turbulent intensity above which the evolution of a turbulent flame can be expected to be dominated by cusps, thereby, leading to values of I substantially larger than unity. Consider a section of an idealized curved flame front containing a cusp and perturbed with a wavelength λ_c and an amplitude l_c , schematically shown in Fig. 14. This type of structure was considered by Zel'dovich [25] as a model of the flame formed under the action of the Landau-Darrieus instability in order to analyze the stabilizing effect of cusps. Such idealized flame, however, can develop under the action of any destabilizing process, e.g., the Rayleigh-Taylor instability or, in our case, turbulence. In particular, Fig. 14 can represent the flame surface deformed by two adjacent counter-rotating vortices of size λ_c .

As discussed in § 5.3 (Fig. 12), the speed of cusp propagation, D_c , (Fig. 14) is much larger than both S_L and the maximum local flame speed in the cusp, S_l^* . Moreover, unlike S_l^* , $D_c \gg S_L$ even at large flame inclination angles, and, thus, it increases gradually with curvature. Therefore, D_c is the primary factor responsible for decreasing the amplitude of the cusp and smoothing the flame surface. In particular, the rate of decrease of the cusp amplitude is [25]

$$\left(\frac{dl_c}{dt}\right)_- = -S_L \left(\frac{1}{\sin \alpha} + 1\right). \quad (24)$$

The angle α and, thus, $(dl_c/dt)_-$, will change with the cusp amplitude. In order to relate α and l_c , a parabolic shape of the flame was assumed in [25], and eq. (24) can then be rewritten as

$$\left(\frac{dl_c}{dt}\right)_- = -8S_L \frac{l_c^2}{\lambda_c^2}. \quad (25)$$

The net rate of change of l_c is determined by the balance of the stabilizing process described by eq. (25) and a destabilizing one, which gives

$$\frac{dl_c}{dt} = \Psi - 8S_L \frac{l_c^2}{\lambda_c^2}. \quad (26)$$

In the turbulent flow, flame perturbations can be assumed to grow linearly in time as they are being stretched by the turbulent speed U_λ characteristic of the scale λ_c . This gives the growth rate $\Psi = U_\lambda$. By setting $dl_c/dt = 0$, the limiting value of $l_c(\lambda_c)$ can be determined. It was shown by Khokhlov [7] in the context of Rayleigh-Taylor-unstable flames that nonlinear flame stabilization due to cusp propagation can be expected to fail once $l_c \gtrsim \lambda_c$. Therefore, by setting $l_c = \lambda_c$, $\Psi = U_\lambda$, and $dl_c/dt = 0$ in eq. (26), he found the critical value of the turbulent velocity on a given scale λ_c [7]

$$U_\lambda = 8S_L. \quad (27)$$

This is the value of U_λ that is needed to overcome the stabilizing effect of cusps and, thereby, to deform the flame on scale λ_c . This result was used to demonstrate that, in order for the flame to be unstable at a wavelength λ_c under the action of turbulent motions, the turbulent speed on that scale must be substantially larger than S_L [7].

This shows that given a specific turbulent cascade, the flame will be smooth on scales smaller than some critical wavelength λ_c^* on which the condition in eq. (27) is satisfied. It was shown above that in order for the cusps to have a pronounced effect on the flame evolution, the flame must be folded on scales comparable to the full flame width l_F ,

which in our case is $\approx 2\delta_L$. Therefore, by setting $\lambda_c^* = l_F$ and using eq. (27), we find that the flame will be curved on scales $\sim l_F$ when turbulent velocity on that scale becomes $\approx 8S_L$. In a turbulent flow with the Kolmogorov energy spectrum, the corresponding critical value of the integral turbulent velocity then is

$$U_l^* \approx 8S_L \left(\frac{l}{l_F} \right)^{1/3}. \quad (28)$$

This gives the critical values of the Karlovitz number, Ka^* , and the Damköhler number, Da^* , written using their traditional definitions [10]

$$\begin{aligned} Ka^* &= \frac{t_F}{t_\eta} = \left(\frac{l_F}{L_G} \right)^{1/2} = 8^{3/2} \approx 20, \\ Da^* &= \frac{t_T}{t_F} = \frac{lS_L}{l_F U_l} = \frac{1}{8} \left(\frac{l}{l_F} \right)^{2/3}. \end{aligned} \quad (29)$$

Here $t_F = l_F/S_L$ is the characteristic flame time, t_η is the Kolmogorov time, $t_T = l/U_l$ is the characteristic turbulent time on the integral scale, and $L_G = l(S_L/U_l)^3$ is the Gibson scale.

The range of the regimes, in which l is expected to be larger than unity according to the eq. (28), is shown on a traditional combustion regime diagram [10] in Fig. 15 as the orange region. The filled red square corresponds to the simulations presented here. We also determined the time-averaged value of l in a simulation with approximately twice lower turbulent intensity which, however, was still above the $Ka \approx 20$ line. In this calculation, which is represented with the open red square in Fig. 15, we found $\bar{l}_{0.15} \approx 1.16$. Details of this calculation will be presented in a separate paper.

Despite the simplicity of the cusp model used here, eqs. (28)-(29) provide a rather accurate criterion for the onset of the cusp-dominated regime of the turbulent flame evolution. In particular, the decrease in the value of $\bar{l}_{0.15}$ between the two turbulent intensities considered in Fig. 15 suggests that below the $Ka \approx 20$ line, l deviates from unity at most by a few percent. Consequently, this line can be viewed as an approximate upper range of validity of Damköhler's concept.

5.6. Nonlinear regime of turbulent flame evolution

Finally, how will the distribution of S_T/S_L as a function of $A_{0.15}/L^2$ shown in Fig. 5b vary with the change in turbulent intensity?

Based on the model discussed in § 5.3-5.4, the total turbulent flame speed can be viewed as consisting of two components. The first is the contribution of the smoothly curved flame regions with the curvature radius $> \delta_L$ in which $S_l = S_L$. The second is the effect of cusps. Since $S_l > S_L$ in cusps, their contribution depends nonlinearly on the flame surface area contained in them, as evidenced by Figs. 13.⁶ Therefore, the total fuel-consumption speed of the turbulent flame can be written as $\dot{m}_R/\rho_0 = (1 - f_c)S_L A_T + f_c S_L \mathcal{F}'(A_T)$, where $\mathcal{F}'(A_T)$ is some nonlinear function, and f_c is the fraction of the flame surface area contained in cusps. This can be rewritten in terms of S_T defined in eq. (10) as

$$\frac{S_T}{S_L} = (1 - f_c) \frac{A_T}{L^2} + f_c \mathcal{F} \left(\frac{A_T}{L^2} \right) = \frac{A_T}{L^2} + \tilde{\mathcal{F}} \left(\frac{A_T}{L^2} \right), \quad (30)$$

where \mathcal{F} and $\tilde{\mathcal{F}}$ are nonlinear functions.

The balance between the linear and nonlinear terms in eq. (30) is controlled by f_c and, therefore, by the rate of cusp creation, $(d(f_c A_T)/dt)_+$. The following qualitative physical model can be used to estimate this rate (see also [7]). Consider a structure consisting of planar flame sheets, as was discussed in § 5.4. If the flame surface density of such configuration is Σ_T , then the average flame separation is $1/\Sigma_T$. Such flame sheets will move toward each other with the speed $S_L + U_T$, where U_T is some characteristic turbulent velocity responsible for the advective transport of the flame. Since U_l is the largest velocity of coherent turbulent motions, then U_T can be approximated with U_l . Consequently, the flame sheets will merge and annihilate in the time $t_c \sim 1/(\Sigma_T(S_L + U_l))$. The quantity $(d(f_c A_T)/dt)_+$ will depend on the total surface area of the flame sheets times the frequency of their collisions, i.e., $(d(f_c A_T)/dt)_+ \propto A_T/t_c \propto A_T \Sigma_T (S_L + U_l)$. While, in principle, the change in Σ_T does not imply a similar change in A_T , and vice versa, it was shown in § 4.3 that A_T and Σ_T are well correlated. Therefore, A_T can be viewed as simply proportional to Σ_T and, thus, finally

$$\left(\frac{d(f_c A_T)}{dt} \right)_+ \propto (S_L + U_l) \Sigma_T^2 \propto (S_L + U_l) A_T^2. \quad (31)$$

⁶Note that the flame surface area of the configuration shown in Fig. 10 does not depend on α and is a function only of l_c .

Note that this expression is very similar to the destruction term often used in the balance equation of the flame surface density (see [28] for a review of a number of such models). This is also analogous to the rate of collisions of gas molecules with Σ_T playing the role of number density and the turbulent intensity playing the role of temperature in determining the speed with which constituents approach each other.

In § 5.4 we noted that in the actual turbulent flame, there will exist other types of flames collisions besides the ones that can be represented with planar flame sheets. Such configurations will result in an even faster rate of cusp creation that would likely be proportional to the higher powers of Σ_T and, possibly, U_l . The probability of the formation of such flame collisions, however, will rapidly decrease with the increase in their complexity [3, 7].

Eq. 31 shows that the flame surface area contained in cusps in the turbulent flame grows faster than the total A_T . Consequently, with increasing A_T and Σ_T , the balance in eq. (30) shifts rapidly toward the nonlinear term associated with cusps.

This picture then shows how the distribution of S_T/S_L as a function of A/L^2 , given in Fig. 5b, changes with turbulent intensity. At a specific U_l , a variety of different flame configurations with different values of A_T and Σ_T are realized in the course of flame evolution. Larger values of A_T lead to larger Σ_T , which increases the frequency of occurrence of cusps, i.e., f_c . As a result, the nonlinear term in eq. (30), which rapidly grows with A_T , begins to dominate, and this causes a progressively more exaggerated response of S_T to the increase in A_T . Moreover, since a flame with a given surface area can exist in a variety of configurations with different numbers and types of cusps, this creates a scatter in the distribution of S_T/S_L vs. A_T/L^2 .

At lower turbulent speeds, the distribution of S_T/S_L vs. A_T/L^2 should collapse onto the $S_T/S_L = A_T/L^2$ line since, in the limit of complete absence of cusps, there is a unique correspondence between these two quantities. Eq. (30) suggests that such behavior would indeed take place. As U_l becomes smaller, the flame will be less convolved, causing the center of mass of the distribution to shift toward smaller values of A_T/L^2 and, thus, S_T/S_L . Since the surface area contained in cusps depends not only on A_T but also on U_l (eq. (31)), smaller U_l will cause the cusps to be less prevalent at a fixed A_T/L^2 . As a result, the nonlinear term in eq. (30), will be smaller and the overall distribution S_T/S_L vs. A_T/L^2 will be closer to the $S_T/S_L = A_T/L^2$ line. Moreover, since all potential statistical variations in the distribution are associated with cusps and are, thus, represented by the nonlinear term $\tilde{\mathcal{F}}(A/L^2)$, the decrease in the latter will also lead to the decrease in the distribution scatter.

At larger U_l , the behavior will be opposite. The center of mass of the distribution will shift to larger values of A_T/L^2 and S_T/S_L . The nonlinear term in eq. (30) will become progressively more dominant, causing larger values of S_T/S_L at a given A_T/L^2 and, thus, enhancing the exaggerated response of S_T .

As the turbulent intensity increases, the overall distribution of S_T/S_L vs. A_T/L^2 will not only deviate more strongly from the $S_T/S_L = A_T/L^2$ limit, but it will also become more pronouncedly curved upward. This is the result of the fact that

$$\frac{d^2\overline{S}_T(A_T)}{dA_T^2} > 0 \quad (32)$$

and the magnitude of $d^2\overline{S}_T(A_T)/dA_T^2$ at every point increases as U_l becomes larger. Here $\overline{S}_T(A_T)$ represents the time-averaged value of S_T in the limit of large statistics.

To show that inequality (32) holds, consider first the limiting value of Σ_T . The fact that the flame is not an infinitely thin surface means that such limit does exist. Once Σ_T becomes large enough so that the individual flame sheets come into contact, Σ_T cannot increase beyond that. This maximum value $\Sigma_{T,max}$ can be estimated assuming that the minimum flame separation is equal to the full flamelet width l_F , which in our case is $\approx 2\delta_L$ (cf. Fig. 7 in [9]). Then⁷

$$\Sigma_{T,max} \equiv \Sigma_{0.15,max} = \frac{1}{2\delta_L} \approx 1.5 \text{ mm}^{-1}. \quad (33)$$

It was discussed in [9], based on the comparison of the results of that work with the results of Aspden et al. [29], that the turbulent flame width, δ_T , is primarily determined by the integral scale, l , (and, therefore, by the driving scale, L). A similar conclusion was also reached by Peters [10] (cf. eq. (2.175) therein). If L is held fixed, then l will also remain constant as the turbulent intensity increases. Consequently, δ_T will not change with increase in U_l . Substituting the value of $\overline{\delta}_T$ obtained in simulation S3 (see Table 3) into eq. (18), and setting $\Sigma_T = \Sigma_{T,max}$, the corresponding maximum value of the flame surface area is

$$\frac{A_{T,max}}{L^2} \equiv \frac{A_{0.15,max}}{L^2} \approx 7.2. \quad (34)$$

Part of the increase in A_T is typically associated with the increase in δ_T and not only Σ_T . Therefore, actual values of $A_{T,max}/L^2$ can be somewhat larger than the one given above. Thus eq. (34) should be viewed as a more approximate limit than eq. (33).

⁷Note that $\Sigma_{T,max}$ is different from Σ_{max} typically used in combustion research and discussed in § 4.1.

The situation when all of the flame surface is in contact with itself corresponds to the infinite local flame speed and, thus, infinite S_T . Therefore, as $A_T/L^2 \rightarrow A_{T,max}/L^2$, both $S_T/S_L \rightarrow \infty$ and $d\bar{S}_T/dA_T \rightarrow \infty$. On the other hand, at small values of A_T/L^2 , the slope of \bar{S}_T is finite and, in fact, as $A_T/L^2 \rightarrow 1$, $d\bar{S}_T/dA_T \rightarrow S_L/L^2$. This shows that the slope of the distribution S_T/S_L cannot be constant and instead $d\bar{S}_T/dA_T$ has to be a monotonically increasing function, which proves the inequality (32). Since this inequality is the consequence of the creation of cusps in the turbulent flame, the magnitude of $d^2\bar{S}_T(A_T)/dA_T^2$ will increase with increase in the frequency of creation of cusps and, thus, with increase in both A_T and U_l . Therefore, as turbulent intensity becomes larger, the curvature of the distribution will become pronounced at progressively lower values of A_T .

6. Conclusions

This work continued the analysis of the set of three numerical simulations first presented in [9]. These calculations model the interaction of the premixed flame with high-speed, subsonic, homogeneous, isotropic turbulence in an unconfined system, i.e., in the absence of walls and boundaries. The turbulent r.m.s. velocity, U_{rms} , is ≈ 35 times larger than the laminar flame speed, S_L . The resulting Damköhler number based on the turbulent integral scales is $Da = 0.05$. It was demonstrated in [9] that this system represents turbulent combustion in the thin reaction zone regime. Even in the presence of such intense turbulence, the turbulent flame consists of highly convolved flamelets with the reaction-zone structure virtually identical to that of a planar laminar flame and with the preheat zone broadened by a factor ≈ 2 .

The fact that turbulence is unable to penetrate and disrupt the internal flame structure showed that diffusive processes are not enhanced on small scales by turbulent transport, and flamelets propagate locally with the speed of the planar laminar flame [9]. This raised the following question: Can the magnitude of the turbulent flame speed in the presence of high-intensity turbulence be fully accounted for by the increase in the flame surface area, as was originally suggested by Damköhler [1]? Here we summarize the main findings of our study of this issue.

Analysis of the area and density of the fuel mass-fraction isosurfaces, $A(Y)$ and $\Sigma(Y)$, showed that the flamelet, folded inside the flame brush in the presence of high-speed turbulence, cannot be viewed as a thin uniform structure, in which all isosurfaces are parallel to each other. Different regions of the flamelet have quite different response to the action of turbulence. In the higher-resolution calculations S2 and S3, both A and Σ , on average, increase monotonically through the flamelet with decreasing temperature, which is manifested in the distinctive inverted-S shape of their time-averaged distributions. As a result, isosurfaces of higher fuel mass fractions are folded by turbulence on progressively smaller scales. This causes the substantially finer wrinkling of the flame surface on the fuel side than on the product side observed in [9].

Distributions of $\bar{A}(Y)$ and $\bar{\Sigma}(Y)$ showed that in the presence of the high-speed turbulence considered here, the definition of the flame surface area, A_T , must be revisited before the balance between A_T and the turbulent flame speed, S_T , can be considered. In particular, it must be determined which value of Y characterizes the evolution and global properties of the turbulent flame most fully and accurately. In order to answer this question, we analyzed the correlation of $A(Y)/L^2$ with quantities that characterize both the energetics and the global structure of the turbulent flame, namely its normalized speed, S_T/S_L , and width, δ_T/L . We also analyzed the correlation of $\Sigma(Y)$ with S_T/S_L . This analysis demonstrated that global properties of the turbulent flame are best represented by the structure of the region of peak reaction rate. For the reaction-diffusion model used in this work, this corresponds to $Y \approx 0.15$. Therefore, the isosurface of this value of Y must be viewed as the flame surface and $A_T = A_{0.15}$.

Larger values of A_T are associated with larger flame surface density, Σ_T . In other words, A_T grows primarily as a result of the much tighter folding and packing of the flame, rather than only due to the increase in the overall width of the flame brush. Given the absence of any broadening of the reaction zone observed in [9], this shows that high-intensity turbulence is much more efficient at tightly packing the flamelets inside the flame brush rather than at disrupting and broadening their internal structure (also see [10]).

Consideration of the stretch factor, I , calculated at $Y = 0.15$, and, more generally, of the distribution of S_T/S_L vs. $A_{0.15}/L^2$ led to the following key conclusion of this work: In the presence of high-speed turbulence, the magnitude of the turbulent flame speed cannot be attributed purely to the increase in the flame surface area. In particular, in the highest-resolution simulation S3 at all times $I_{0.15} > 1$ and, thus, $S_T/S_L > A_{0.15}/L^2$. The deviation of $I_{0.15}$ from unity is, on average, $\approx 30\%$ and occasionally reaches as high as 50% . Since the local flame speed is not increased by turbulence [9], this shows that Damköhler's concept breaks down for sufficiently high-intensity turbulence, even for the flows characterized by $Le = 1$.

The deviation of S_T/S_L from A_T/L^2 becomes larger as A_T and Σ_T increase. In other words, an increase in the flame surface area, and the associated tighter packing of the flame, result not just in a larger turbulent flame speed but, most importantly, in the progressively more exaggerated response of S_T to the increase in A_T . This causes substantially accelerated burning.

Tightly packed flame configurations, produced by high-speed turbulence, result in frequent flame collisions, which lead to the formation of regions of high flame curvature $\gtrsim 1/\delta_L$, or “cusps.” This results in significant focusing of the thermal flux over an extended region of the flame surface which increases the local flame speed in the cusp, S_l , over its laminar value, S_L . Due to the large values of S_l , the contribution of cusps to the total S_T is disproportionately large compared to the flame surface area in them. This provides a natural mechanism for the formation of the exaggerated response of S_T . The increase of S_l in cusps is inherently local, and it does not require flame broadening and acceleration by turbulent transport, in agreement with the results of [9].

Our results suggest that there exist two distinct regimes of flame evolution. At low turbulent intensities, the turbulent flame evolves in the linear regime. Here the role of cusps, and thus of the nonlinear term in eq. (30), is negligible and $S_T \propto A_T$. High turbulent velocities mark the onset of the nonlinear regime, which is dominated by cusps formed in the tightly packed turbulent flame. The nonlinear increase of S_l in cusps, and, therefore, the nonlinear dependence on A_T of the contribution of cusps to S_T , causes a strong exaggerated response of S_T to the increase in A_T .

The onset of the nonlinear regime of flame evolution marks the breakdown of Damköhler’s concept. Moreover, in this regime, flame propagation can no longer be viewed as a local process. In particular, the local flame speed at each point of the flame surface is no longer determined only by the local thermodynamic state of the flow or by turbulent motions on scales $\lambda < \delta_L$. Instead, in this regime, S_l is also determined by long-range velocity correlations, which produce flame collisions and can span the full size of the system.

Both the criteria given by eqs. (27)-(29) and the results of numerical simulations show that the transition to the nonlinear regime occurs well within the thin reaction zone mode of combustion and, in particular, at $Ka \gtrsim 20$ (Fig. 15). Above this critical value of Ka , the flame evolution likely remains in the nonlinear regime at all turbulent intensities, since the turbulence is more efficient at packing the flame than at broadening it. In particular, at high enough values of U_l , turbulence will eventually break the internal flame structure, which will increase the local flame speed. This will, in turn, make the right-hand side of eq. (27) larger, thereby, enhancing the stabilizing effect of cusps. On the other hand, the flame width, l_F , will also grow, increasing the critical flame separation necessary for the onset of the nonlinear regime. Since S_l is determined by smaller-scale turbulence, while flame folding is governed by the faster larger-scale motions, it is unlikely that S_l can grow fast enough to compensate for the increase in both l_F and the turbulent speeds which fold the flame. Consequently, at higher U_l , i.e., even in the broken reaction zone mode, the linear regime most likely cannot be recovered. This issue, however, requires further investigation in future studies.

The increase of S_l in cusps is discussed here for $Le = 1$. It is well known, however, that when $Le \neq 1$, S_l can increase with the curvature of the flame [3]. Therefore, due to the large flame curvature in cusps, any imbalance between thermal and diffusion fluxes can significantly exacerbate the enhancement of S_l . Consequently, the exaggerated response of S_T , discussed here, can be substantially larger for the reactive flows characterized by $Le \neq 1$.

Results presented in this work show that for the large range of turbulent intensities and system sizes, knowledge of A_T is no longer sufficient to predict the magnitude of S_T . For instance, at the turbulent speeds considered here, using A_T as a guide results in errors on the order of 30 – 50%. Such errors are quite substantial given that the flow evolution is typically very sensitive to the rate of energy release. Therefore, it is particularly important to account for the nonlinear effects in subgrid-scale models that primarily focus on determining the evolution of A_T (e.g., [7]).

Furthermore, the formation of cusps and the resulting rapid flame propagation in certain regions is a crucial part of the turbulent flame-brush evolution in the high-speed regime. Thus, properly capturing this regime in numerical models requires the domain size to be larger than the integral scale in order to accommodate the folding of the flame by turbulence. Making the domain smaller than l would significantly hamper this process, while making the domain smaller than $\sim \delta_L$ would completely eliminate it.

Finally, two possibilities exist for the flame evolution in the nonlinear regime. If the turbulent intensity is not too high, an equilibrium is established between flame-surface creation and its rapid destruction in cusps. This results in the turbulent flame propagating in a steady state, which is the situation observed here. On the other hand, if the turbulent intensity continues to rise, eventually Σ_T and A_T will approach their limiting values given by eqs. (33)–(34). In this regime, as was discussed in § 5.6, both S_T and dS_T/dA_T can become arbitrarily large. Such singular behavior suggests that, in reality, at some point the steady state ceases to exist and the system must undergo a qualitative transformation in order to accommodate the rise in S_T or, equivalently, in the rate of energy release per unit volume. Such qualitative change may indicate the transition from the deflagration to a detonation. Detailed discussion of this non-steady regime will be presented in a separate paper.

Acknowledgments We thank Vadim Gamezo, Forman Williams, Craig Wheeler, Jim Driscoll, Ken Bray, and Matthias Ihme for stimulating discussions in the course of this work. This work was supported in part by the National Research Council Research Associateship Programs in cooperation with the Naval Research Laboratory, by the Office of Naval Research, by the Air Force Office of Scientific Research under the grant FIATA09114G005, and by the National

Science Foundation through TeraGrid resources provided by NCSA and TACC under the grant TG-AST080006N. Additional computing facilities were provided by the Department of Defense High Performance Computing Modernization Program.

Appendix A. Definition of the flame surface density

The definition of $\Sigma(Y)$, given in eq. (18), relied on the isosurface area normalization by the full width of the flame brush. It is, however, not clear *a priori* whether all isosurfaces occupy the full interior of the flame brush and are not confined to a smaller part of it. Consider Fig. 2. It can be seen that neither the $Y = 0.05$, nor the $Y = 0.95$ isosurface extend over the full width of the flame brush, and they indeed occupy a smaller volume.

In order to give this a more quantitative representation, we define $z_{0,max}$ and $z_{1,min}$ by analogy with $z_{0,min}$ and $z_{1,max}$ that were used to specify δ_T in eqs. (9)-(10). In particular,

$$\begin{aligned} z_{0,max} &= \min(z) : Y(x, y, z) > 0.05 \quad \forall (x, y, z > z_{0,max}), \\ z_{1,min} &= \max(z) : Y(x, y, z) < 0.95 \quad \forall (x, y, z < z_{1,min}). \end{aligned} \quad (35)$$

In other words, $z_{0,max}$ is the z -coordinate of the rightmost cell with pure product, while $z_{1,min}$, respectively, is the z -coordinate of the leftmost cell with pure fuel. Thereby, $z_{0,max}$ and $z_{1,min}$ effectively measure the furthest extent of product and fuel penetration into the flame brush. Given the definitions of $z_{0,min}$ and $z_{1,max}$, provided in § 2.2, $z_{0,min}$ and $z_{0,max}$ bound the volume confining the $Y = 0.05$ isosurface, while $z_{1,min}$ and $z_{1,max}$ bound the $Y = 0.95$ isosurface. At the same time, if $z_{1,min} < z_{0,max}$, these two variables bound the region of macroscopic mixing of product and fuel in the flame brush, i.e., the region in which both pure fuel and pure product can be found. Fig. 2 provides the illustration of all four of these quantities.

Next, we define the position of the turbulent flame brush as

$$z_T = \frac{z_{0,min} + z_{1,max}}{2}. \quad (36)$$

Modified $\tilde{z}_{0,max}$ and $\tilde{z}_{1,min}$ are then defined as offsets of $z_{0,max}$ and $z_{1,min}$ with respect to z_T normalized by δ_T , namely

$$\tilde{z}_{0,max} = \frac{z_{0,max} - z_T}{\delta_T}, \quad \tilde{z}_{1,min} = \frac{z_{1,min} - z_T}{\delta_T}. \quad (37)$$

Thus, $\tilde{z}_{0,max}$ and $\tilde{z}_{1,min}$ are the relative measure of the extent to which pure fuel and pure product penetrate into the flame brush. It follows from the definition (37), that both quantities take on values in the interval $[-0.5, 0.5]$. For example, in a planar laminar flame, they are constant with $\tilde{z}_{0,max} = -0.5$, $\tilde{z}_{1,min} = 0.5$. In the turbulent flame brush, zero values would indicate that both fuel and product reach the midpoint of the flame brush, they are confined to the left and right halves of the brush, and there is no macroscopic mixing of fuel and product. If $\tilde{z}_{0,max} = 0.5$ and $\tilde{z}_{1,min} = -0.5$, then both pure product and pure fuel can be found throughout the entire volume of the flame brush.

Fig. 16 shows the evolution of $\tilde{z}_{0,max}$ and $\tilde{z}_{1,min}$ for simulations S1 - S3. In all cases, both parameters exhibit fairly similar evolution oscillating around zero. Overall, pure fuel and product tend to be separated in the flame brush. As the system evolves, however, it undergoes recurring transitions between periods of enhanced fuel-product mixing and episodes of their near complete separation. The correlation between these quantities and S_T is much less prominent compared, for instance, with that between $A(Y)$ and S_T , although it is possible to associate some peaks and troughs with the corresponding changes in the turbulent flame speed.

It follows from Fig. 16 that throughout the course of the simulation, both the $Y = 0.05$ and $Y = 0.95$ isosurfaces occupy the region smaller than the full flame-brush volume. This is also the case for other isosurfaces (cf. Fig. 2). Consequently, an argument can be made that when calculating $\Sigma(Y)$, normalization should be performed not over the full volume of the flame brush, but rather over the respective volume bounding the given isosurface. For instance, for $Y = 0.05$ this volume is $L^2(z_{0,max} - z_{0,min})$. Such definition of $\Sigma(Y)$ would be a more accurate measure of how tightly a given isosurface is folded. Fig. 16 shows that, on average, both the $Y = 0.05$ and $Y = 0.95$ isosurfaces are confined to about half of the total volume of the flame brush. Then with this modified definition of Σ , its corresponding values in Figs. 7-8 should be multiplied by a factor of two. Ultimately, however, we are interested in determining how the overall flamelet, rather than individual isosurfaces, is folded inside the flame brush since only the flamelet as a whole has actual physical significance. Therefore, we find that the uniform normalization over the total volume occupied by the flamelet represents a more physically grounded choice.

Further motivation for our choice of normalization in the definition of Σ (18) comes when one considers how the values of $\tilde{z}_{0,max}$ and $\tilde{z}_{1,min}$ would change for larger system sizes. Pure fuel and product are always separated by the full width of the flamelet. In particular, in our system the characteristic distance between the points $Y = 0.05$ and $Y = 0.95$

in the flamelet structure is $\approx 2\delta_L$ (see Fig. 7 in [9]). It then follows that

$$z_{1,max} - z_{0,max} \gtrsim 2\delta_L, \quad z_{1,min} - z_{0,min} \gtrsim 2\delta_L. \quad (38)$$

Using eqs. (8), (36), and (37), inequalities (38) can be transformed into the following conditions which must be satisfied at each moment in time

$$\tilde{z}_{0,max} \lesssim 0.5 - \frac{2\delta_L}{\delta_T}, \quad \tilde{z}_{1,min} \gtrsim -0.5 + \frac{2\delta_L}{\delta_T}. \quad (39)$$

Horizontal dashed lines in Fig. 16 show the average limiting $\tilde{z}_{0,max}$ and $\tilde{z}_{1,min}$ based on the values of $\bar{\delta}_T/\delta_L$ listed in Table 3 for each simulation. In particular, in all three calculations $\tilde{z}_{0,max}$ must be $\lesssim 0.36$ while $\tilde{z}_{1,min}$ must be $\gtrsim -0.36$, which closely agrees with the data shown in Fig. 16.

This demonstrates that both isosurfaces of $Y = 0.05$ and $Y = 0.95$ can never occupy the full volume of the flame brush simply because, by definition, they are separated from the boundary of the flame brush by the flamelet thickness. The latter, in our case, is a substantial fraction of the total flame brush width. It was discussed in § 5.6 that δ_T increases with the turbulent integral scale, or, equivalently, with the system size and energy injection scale ([9], also see [10]). It then follows from eq. (39) that as $\delta_T/\delta_L \rightarrow \infty$, then $\tilde{z}_{0,max} \rightarrow 0.5$ and $\tilde{z}_{1,min} \rightarrow -0.5$. Therefore, in larger systems the flame brush width becomes large in comparison with the width of the flamelet and, as a result, the volume bounding each isosurface becomes well approximated by the total volume of the flame brush. Consequently, in the limit of large values of δ_T , the uniform normalization for all values of Y in eq. (18) becomes equivalent to the normalization by the actual volume bounding a given isosurface.

References

- [1] G. Damköhler, Z. Elektrochemie und Angewandte Physikalische Chemie 46 (1940) 601-626. *English translation:* NASA TM No. 1112 (1947).
- [2] R.W. Bilger, S.B. Pope, K.N.C. Bray, J.F. Driscoll, Proc. Combust. Inst. 30 (2005) 21-42.
- [3] J.F. Driscoll, Prog. Energy Combust. Sci. 34 (2008) 91-134.
- [4] Ya.B. Zel'dovich, Theory of Combustion and Detonation of Gases. Izd-vo AN SSSR, Moscow-Leningrad, 1944.
- [5] C.K. Law, C.J. Sung, Prog. Energy Combust. Sci. 26 (2000) 459-505.
- [6] J.B. Bell, M.S. Day, J.F. Grcar, Proc. Combust. Inst. 29 (2002) 1987-1993.
- [7] A.M. Khokhlov, Astrophys. J. 449 (1995) 695-713.
- [8] E.R. Hawkes, J.H. Chen, Combust. Flame 144 (2006) 112-125.
- [9] A.Y. Poludnenko, E.S. Oran, Combust. Flame 157 (2010) 995-1011.
- [10] N. Peters, Turbulent Combustion, Cambridge University Press, 2000.
- [11] P.A. Libby, F.A. Williams, in: P.A. Libby, F.A. Williams (Eds.), Turbulent Reacting Flows, Academic Press, 1994, 1-61.
- [12] F.A. Williams, in: A. Yoshida (Ed.), Smart Control of Turbulent Combustion, Springer-Verlag, 2001, 1-11.
- [13] V.N. Gamezo, T. Ogawa, E.S. Oran, Combust. Flame 155 (2008) 302-315.
- [14] J.M. Stone, T.A. Gardiner, P. Teuben, J.F. Hawley, J.B. Simon, Astrophys. J. Supp. 178 (2008) 137-177.
- [15] T.A. Gardiner, J.M. Stone, J. Comp. Phys. 227 (2008) 4123-4141.
- [16] P. Colella, J. Comp. Phys. 87 (1990) 171-200.
- [17] J. Saltzman, J. Comp. Phys. 115 (1994) 153-168.
- [18] P. Colella, P.R. Woodward, J. Comp. Phys. 54 (1984) 174-201.
- [19] A.Y. Poludnenko, T.A. Gardiner, E.S. Oran, Naval Research Lab. Memorandum Report (2010), in press.
- [20] A. Kolmogorov, Dokl. Akad. Nauk SSSR 31 (1941) 538-541.
- [21] J.M. Stone, E.C. Ostriker, C.F. Gammie, Astrophys. J. 508 (1998) L99-L102.
- [22] M.N. Lemaster, J.M. Stone, Astrophys. J. 691 (2009) 1092-1108.
- [23] D.A. Frank-Kamenetskii, Diffusion and Heat Transfer in Chemical Kinetics. Nauka, Moscow, 1987.
- [24] L. Pan, J.C. Wheeler, J. Scalo, Astrophys. J. 681 (2008) 470-481.
- [25] Ya.B. Zel'dovich, J. Appl. Mech. & Tech. Phys. 7 (1966) 68-69.
- [26] Ya.B. Zel'dovich, A.G. Istratov, N.I. Kidin, V.B. Librovich, Combustion Sci. Tech. 24 (1980) 1-13.
- [27] L.D. Landau, Zh. Eksperim. i Teor. Fiz. 14 (1944) 6; L.D. Landau, E.M. Lifshitz, Fluid Mechanics, Pergamon Press, Oxford, 1987.
- [28] J.M. Duclos, D. Veynante, T. Poinso, Combust. Flame 95 (1993) 101-117.
- [29] A.J. Aspden, J.B. Bell, M.S. Day, S.E. Woosley, M. Zingale, Astrophys. J. 689 (2008) 1173-1185.

Table 1. Input model parameters and resulting computed laminar flame properties

<i>Input</i>		
T_0	293 K	Initial temperature
P_0	1.01×10^6 erg/cm ³	Initial pressure
ρ_0	8.73×10^{-4} g/cm ³	Initial density
γ	1.17	Adiabatic index
M	21 g/mol	Molecular weight
B	6.85×10^{12} cm ³ /(g s)	Pre-exponential factor
Q	46.37 RT ₀	Activation energy
q	43.28 RT ₀ / M	Chemical energy release
κ_0	2.9×10^{-5} g/(s cm K ⁿ)	Thermal conduction coefficient
D_0	2.9×10^{-5} g/(s cm K ⁿ)	Molecular diffusion coefficient
n	0.7	Temperature exponent
<i>Output</i>		
T_P	2135 K	Post-flame temperature
ρ_P	1.2×10^{-4} g/cm ³	Post-flame density
δ_L	0.032 cm	Laminar flame thermal width
S_L	302 cm/s	Laminar flame speed

Table 2. Parameters of simulations^a

	S1	S2	S3	Description
\mathcal{D}	$64 \times 64 \times 1024$	$128 \times 128 \times 2048$	$256 \times 256 \times 4096$	Domain grid size
\mathcal{D}_A		$1 \times 1 \times 16$		Domain aspect ratio
L		0.259 cm = $8\delta_L$		Domain width, energy-injection scale
Δx	4.05×10^{-3} cm	2.02×10^{-3} cm	1.01×10^{-3} cm	Cell size
$(\overline{\Delta x})^{-1}$	8	16	32	$\delta_L/\Delta x$
$z_{T,0}$		1.95 cm = $7.52L$		Initial flame position along z -axis
ε		1.26×10^9 erg/(cm ³ s)		Energy-injection rate
U_δ		4.53×10^3 cm/s = $15S_L$		Turbulent velocity at scale δ_L
U		9.07×10^3 cm/s = $30S_L$		Turbulent velocity at scale L
U_{rms}		1.04×10^4 cm/s = $34.48S_L$		Turbulent r.m.s. velocity
U_I		5.60×10^3 cm/s = $18.54S_L$		Integral velocity
l		6.04×10^{-2} cm = $1.87\delta_L$		Integral scale
τ_{ed}		2.86×10^{-5} s		Eddy turnover time, L/U
t_{ign}	$3.0\tau_{ed}$	$3.0\tau_{ed}$	$2.0\tau_{ed}$	Time of ignition
t_{total}		$16.0\tau_{ed}$		Total simulation time from t_{ign}
Da		0.05		Damköhler number ^b (l/U_I)/($2\delta_L/S_L$)
L_G		9.47×10^{-6} cm = $2.96 \times 10^{-4}\delta_L$		Gibson scale, $l(S_L/U_I)^3$
Ma_F		0.25		Mach number in fuel, $U(\gamma P_0/\rho_0)^{-1/2}$
Ma_P		0.09		Mach number in product, $U(\gamma P_0/\rho_P)^{-1/2}$

^a Parameters common to all simulations are shown only once in S2 column.

^b In this definition of Da , $2\delta_L$ indicates the full flame width. See [9] for further discussion.

Table 3. Time-averaged properties of the turbulent flame brush^a

	$\bar{\delta}_T/\delta_L$	$O(\bar{\delta}_T/\delta_L)$	\bar{S}_T/S_L	$O(\bar{S}_T/S_L)$	$\bar{A}_{0.15}/L^2$	$O(\bar{A}_{0.15}/L^2)$	$\bar{\Sigma}_{0.15}, \text{mm}^{-1}$	$O(\bar{\Sigma}_{0.15})$	$\bar{I}_{0.15}$	$O(\bar{I}_{0.15})$
S1	16.13		6.09		3.91		0.74		1.52	
S2	14.86	1.96	4.50	2.29	3.23	2.84	0.67	4.07	1.39	1.29
S3	14.42		4.09		3.12		0.67		1.30	

^a Time-averaging for all variables is performed over the time interval $[2\tau_{ed} - 16\tau_{ed}]$.

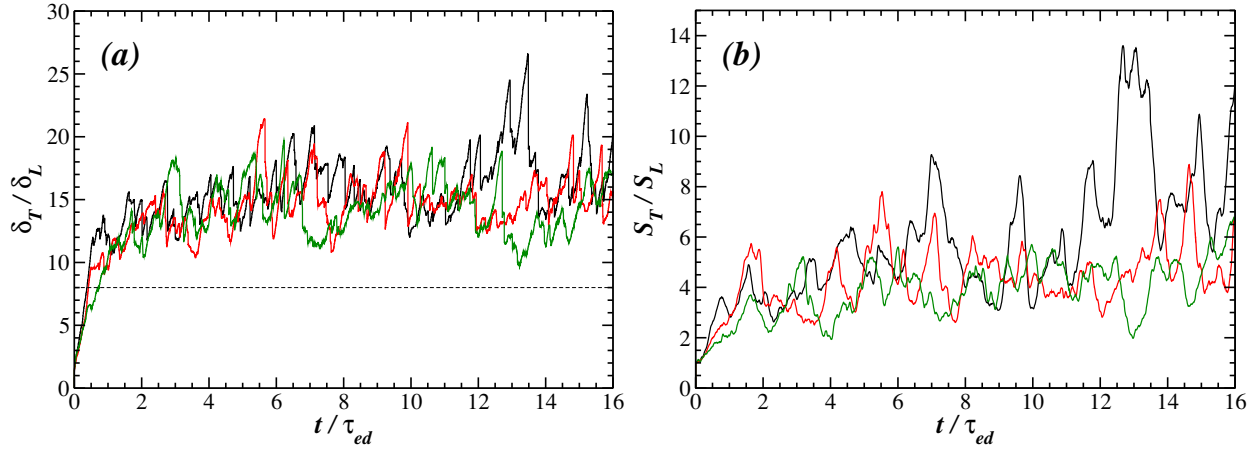


Figure 1 (a) Evolution of the turbulent flame width δ_T normalized by δ_L . Note that domain width $L = 8\delta_L$ indicated with the horizontal dashed line. (b) Evolution of the turbulent flame speed S_T normalized by S_L . In both panels: black lines correspond to simulation S1, red to S2, and green to S3. (Reproduced from [9].)

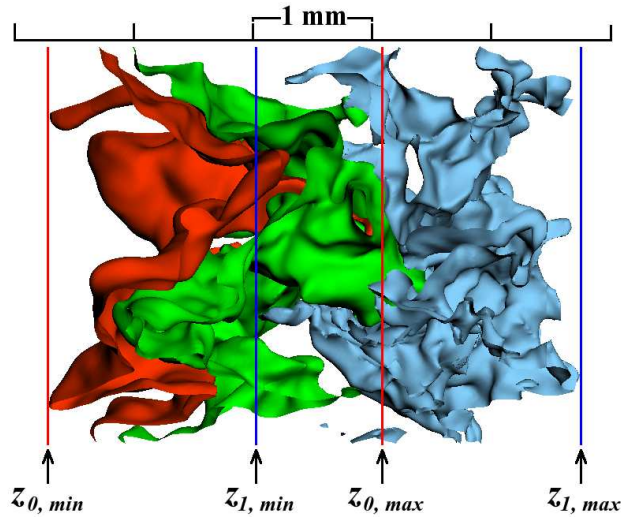


Figure 2 Isosurfaces of Y in simulation S2 at $t = 13\tau_{ed}$ (cf. Fig.3, middle row, left panel in [9]). Isosurface values are 0.05 (red), 0.6 (green), 0.95 (blue). Red and green isosurfaces bound the flamelet reaction zone. Green and blue isosurfaces bound the preheat zone. The $z_{0,min}$ and $z_{1,max}$ mark the flame-brush bounds. The $z_{0,max}$ and $z_{1,min}$ indicate, respectively, the maximum extents of product and fuel penetration into the flame brush (see Appendix A for further discussion of $z_{0,max}$ and $z_{1,min}$). (Reproduced from [9].)

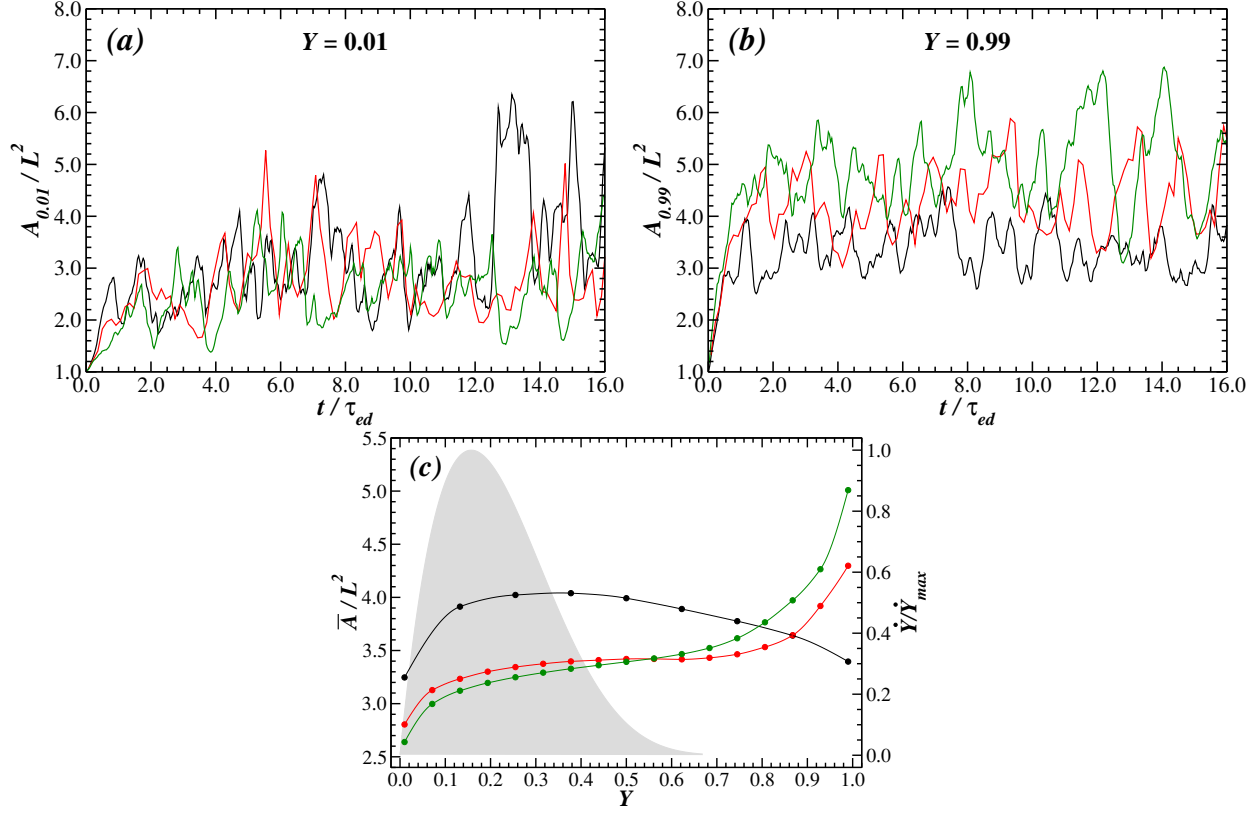


Figure 3 Evolution of the normalized flame surface area (a) $A_{0.01}/L^2$ and (b) $A_{0.99}/L^2$. (c) Time-averaged normalized flame surface area $\bar{A}(Y)/L^2$. Time averaging is performed over the time interval $[2\tau_{ed} - 16\tau_{ed}]$, circles represent calculated values and solid lines are the Akima spline fits. Shaded gray region shows the distribution of the reaction rate, \dot{Y} , in the exact laminar flame solution normalized by its peak value $\dot{Y}_{max} = 9.5 \times 10^4 \text{ s}^{-1}$. In all panels: black corresponds to simulation S1, red to S2, and green to S3.

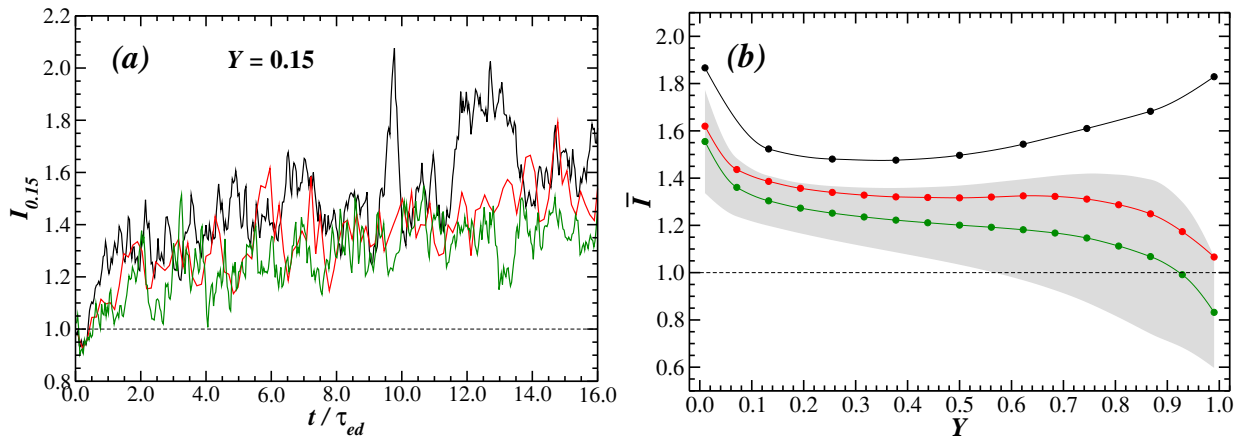


Figure 4 (a) Evolution of the stretch factor $I_{0.15}$. (b) Time-averaged distribution of the stretch factor $I(Y)$. Circles represent calculated values and solid lines are the Akima spline fits. Time averaging is performed over the time interval $[2\tau_{ed} - 16\tau_{ed}]$. The shaded gray area shows $\pm\sigma$ standard deviation of the instantaneous values of $I(Y)$ in simulation S3. In both panels: black corresponds to simulation S1, red to S2, and green to S3.

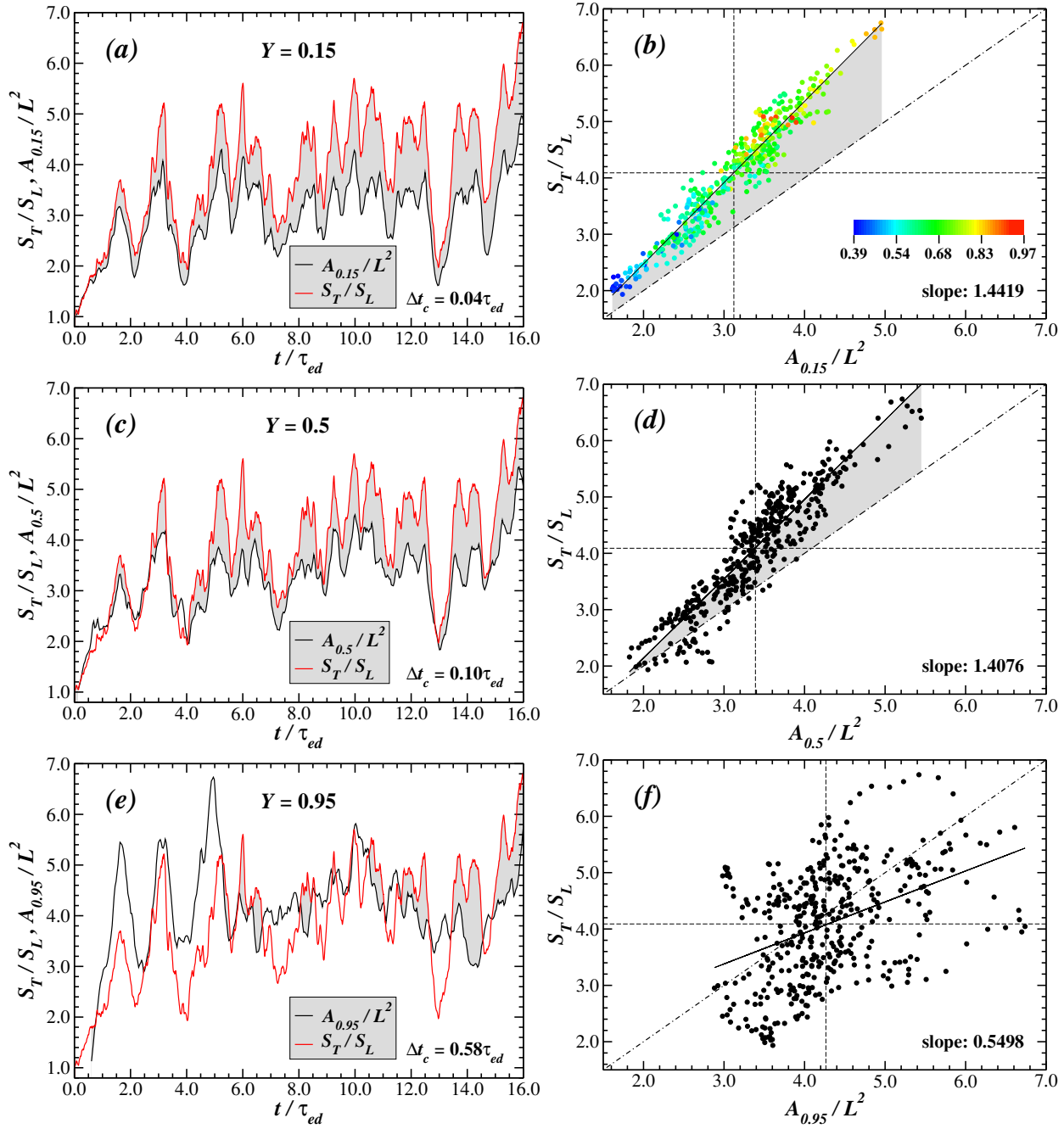


Figure 5 Correlation between $A(Y)/L^2$ and S_T/S_L in simulation S3. $A(Y)$ is considered for three values of Y : (a, b) $Y = 0.15$, (c, d) $Y = 0.5$, and (e, f) $Y = 0.95$. In panels (a), (c), and (e) A/L^2 is shifted in time to the right by the time lag Δt_c shown in each panel. Graphs in panels (b), (d), and (f) are constructed based on the data shown, respectively, in panels (a), (c), and (e) excluding the time $(0 - 2)\tau_{ed}$ during which the turbulent flame develops its equilibrium state. In panel (b) each data point is colored according to the corresponding value of the surface density $\Sigma(Y)$ with the color scale given in units mm^{-1} (cf. Fig. 8a,b). In panels (b), (d), and (f) dashed lines show time-averaged values of A/L^2 and S_T/S_L , solid lines show the least squares fit with its slope given in each panel, and dash-dot lines correspond to $S_T/S_L = A/L^2$. Shaded gray regions in panels (a)-(e) illustrate the exaggerated response of S_T to the increase of A .

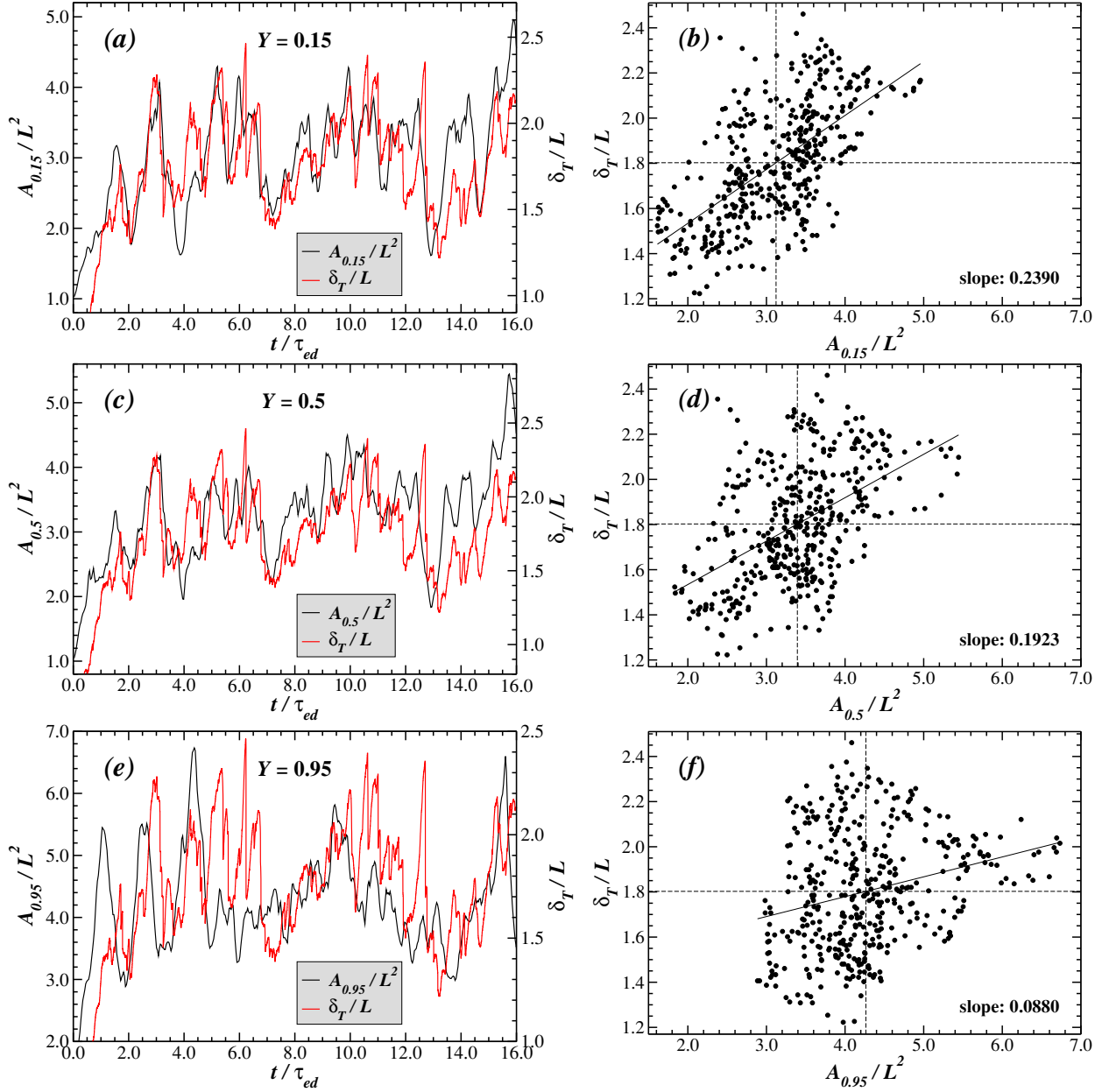


Figure 6 Correlation between $A(Y)/L^2$ and δ_T/L in simulation S3. $A(Y)$ is considered for three values of Y : (a, b) $Y = 0.15$, (c, d) $Y = 0.5$, and (e, f) $Y = 0.95$. Graphs in panels (b), (d), and (f) are constructed based on the data shown, respectively, in panels (a), (c), and (e) excluding the time $(0 - 2)\tau_{ed}$ during which the turbulent flame develops its equilibrium state. In panels (b), (d), and (f) dashed lines show time-averaged values of A/L^2 and δ_T/L , while the solid lines show the least squares fit with its slope given in each panel.

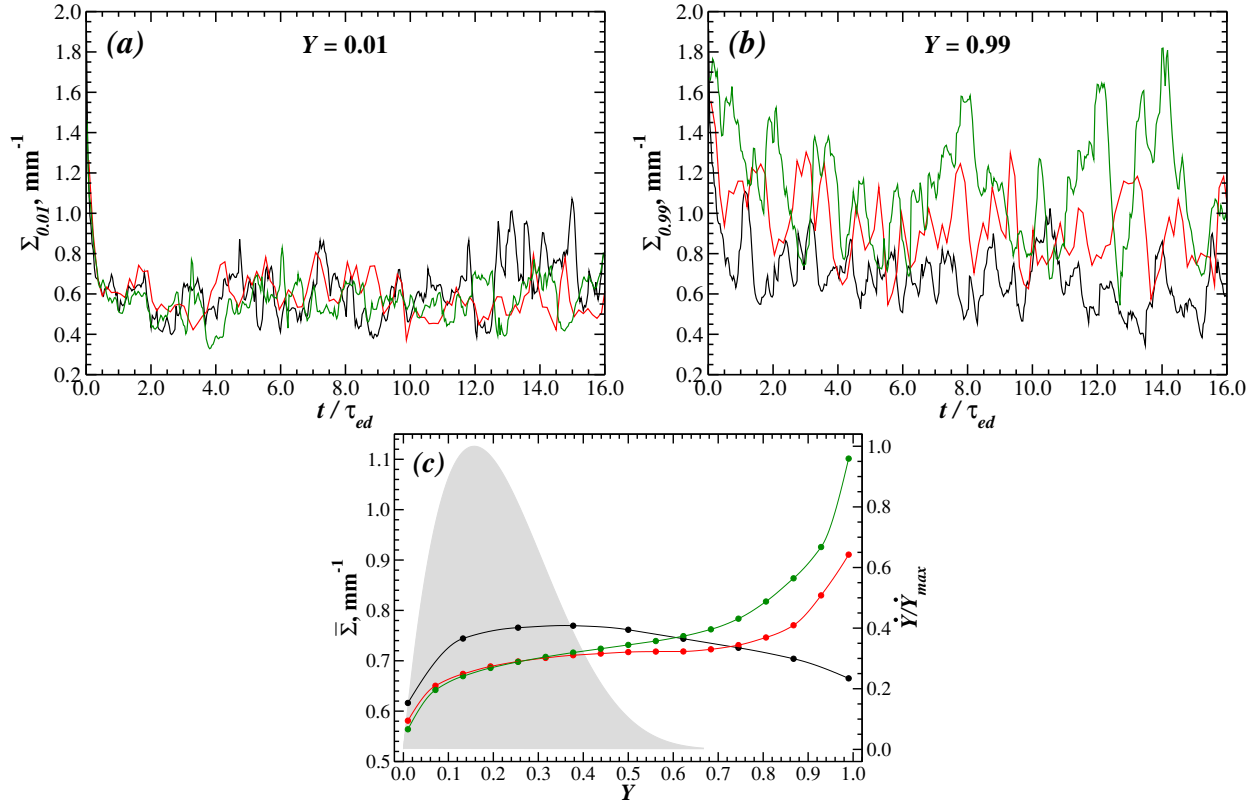


Figure 7 Evolution of the flame surface density (a) $\Sigma_{0.01}$ and (b) $\Sigma_{0.99}$. (c) Time-averaged flame surface density $\bar{\Sigma}(Y)$. Time averaging is performed over the time interval $[2\tau_{ed} - 16\tau_{ed}]$, circles represent calculated values and solid lines are the Akima spline fits. Shaded gray region shows the distribution of the reaction rate, \dot{Y} , in the exact laminar flame solution normalized by its peak value $\dot{Y}_{max} = 9.5 \times 10^4 \text{ s}^{-1}$. In all panels: black corresponds to simulation S1, red to S2, and green to S3.

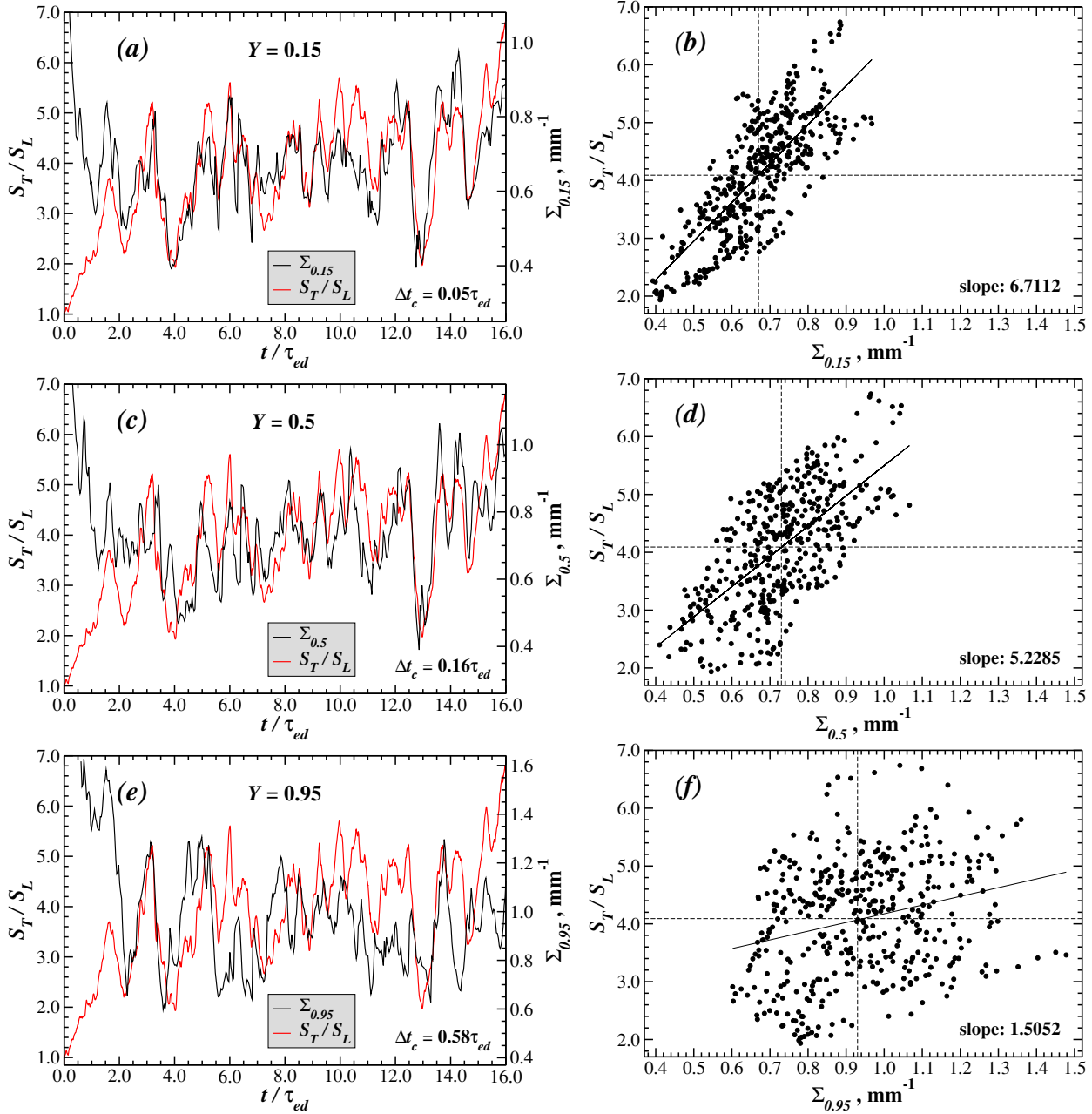


Figure 8 Correlation between $\Sigma(Y)$ and S_T/S_L in simulation S3. $\Sigma(Y)$ is considered for three values of Y : (a, b) $Y = 0.15$, (c, d) $Y = 0.5$, and (e, f) $Y = 0.95$. In panels (a), (c), and (e) Σ is shifted in time to the right by the time lag Δt_c shown in each panel. Graphs in panels (b), (d), and (f) are constructed based on the data shown, respectively, in panels (a), (c), and (e) excluding the time $(0 - 2)\tau_{ed}$ during which the turbulent flame develops its equilibrium state. In panels (b), (d) and (f) dashed lines show time-averaged values of Σ and S_T/S_L , while the solid lines show the least squares fit with its slope given in each panel.

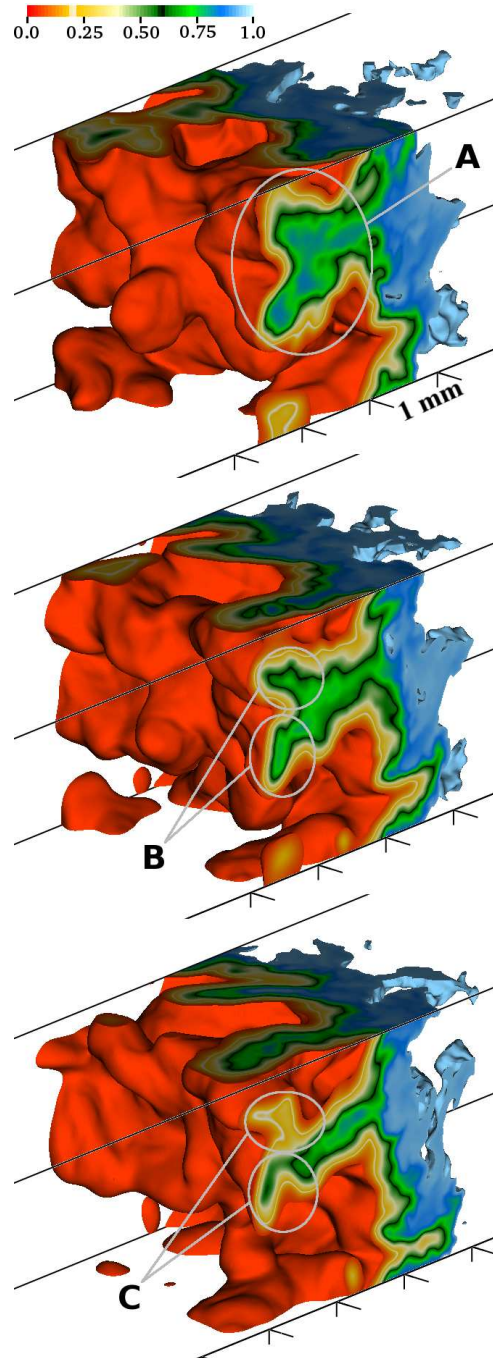


Figure 9 Flame collision and the formation of cusps in the turbulent flame. Shown is the flame-brush structure based on the isovolume of the fuel mass fraction in simulation S3. Bounding isosurfaces represent $Y = 0.05$ and $Y = 0.95$ and the flame brush is shown from the product side. Upper panel corresponds to the time $t = 11.86\tau_{ed}$, while the middle and lower panels show the flame structure, respectively, $0.1\tau_{ed} = 3 \mu\text{s}$ and $0.2\tau_{ed} = 6 \mu\text{s}$ later. The thin black line, corresponding to $Y = 0.6$, marks the boundary between the preheat and reaction zones. The thin white line, corresponding to $Y = 0.2$, shows the location of the peak reaction rate. Regions A, B, and C show the three main stages of the flame collision and the formation of a cusp discussed in § 5.2. Note also two elongated regions of flame collision forming near the upper face of the domain.

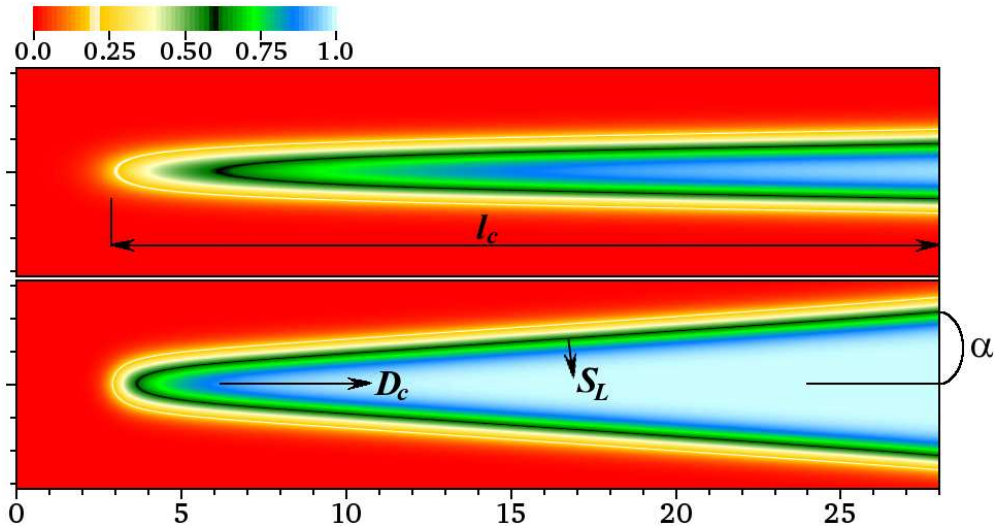


Figure 10 Structure of a cusp formed by the collision of parallel flame sheets. Shown is the distribution of Y for the flame inclination angle $\alpha = 1^\circ$ (upper panel) and $\alpha = 4^\circ$ (lower panel). Scale of the panel axes is given in units of δ_L . Away from the cusp tip, the flame propagates in the direction normal to its surface with the laminar flame speed, S_L , causing the tip to move to the right with the speed D_c . Also shown is the length, l_c , of the collision region (see text). Thin black line marks the boundary between the reaction and preheat zones, while the thin white line indicates the region of peak reaction rate. Note the substantial broadening of the flame, and thus the reaction zone, near the tip of the cusp at $\alpha = 1^\circ$ compared to $\alpha = 4^\circ$ (cf. Fig. 9).

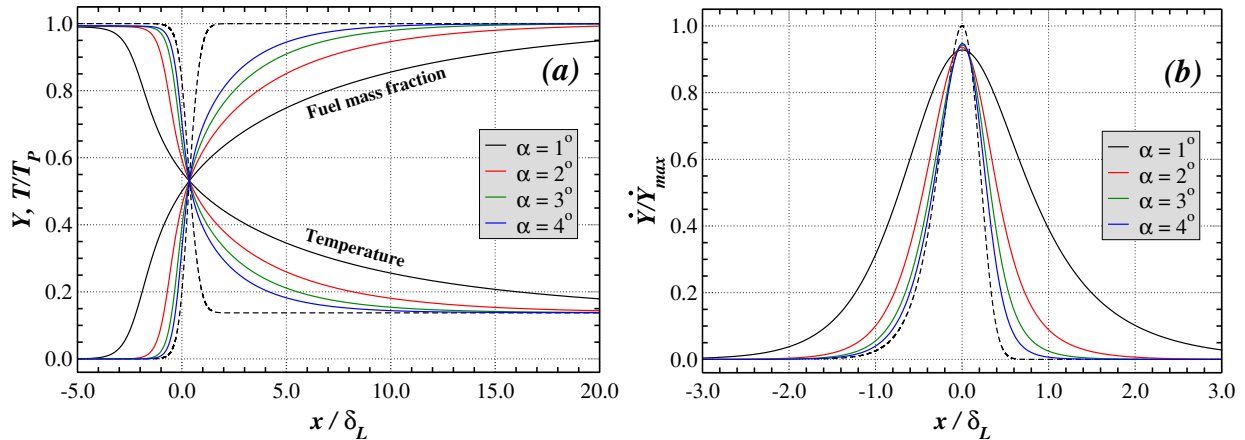


Figure 11 Structure of a cusp formed by the collision of parallel flame sheets for four flame inclination angles, α . Shown are distributions of (a) the fuel mass fraction, Y , and temperature, T , as well as (b) the reaction rate, \dot{Y} , along the symmetry line of the cusp (cf. Fig. 10). Dashed lines in both panels indicate the exact planar laminar flame solution. Profiles of T and \dot{Y} are normalized by their respective maximum values in the exact laminar solution, i.e., T_P (see Table 1) and $\dot{Y}_{max} = 9.5 \times 10^4 \text{ s}^{-1}$.

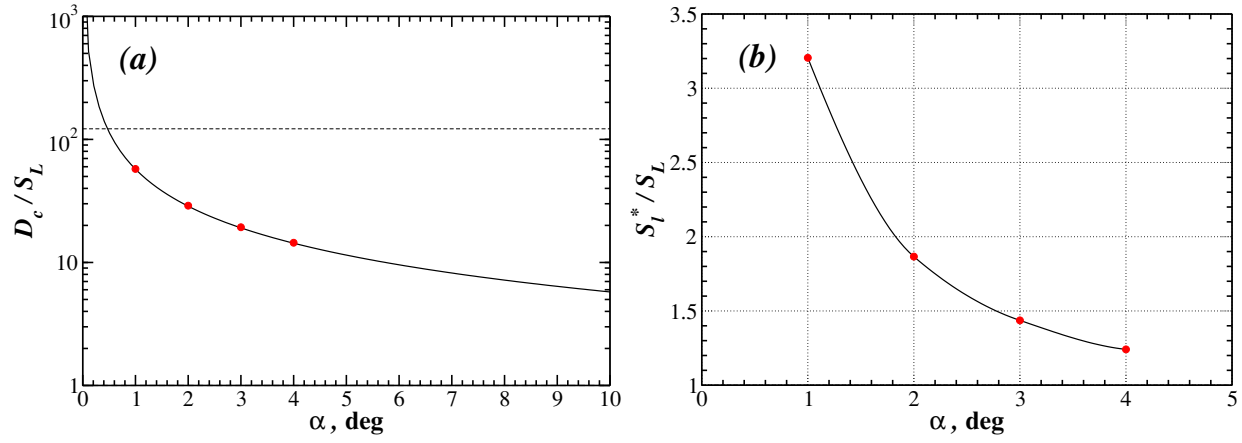


Figure 12 (a) Dependence of the normalized speed of cusp propagation, D_c/S_L , on the flame inclination angle, α . Solid line corresponds to the analytic expression given in eq. (20), red circles show the computed values. Horizontal dashed line indicates sound speed in cold fuel. (b) Dependence of the maximum normalized local burning speed in the cusp, S_l^*/S_L , given by eq. (21), on α . Red circles show the computed values, solid line is the Akima spline fit.

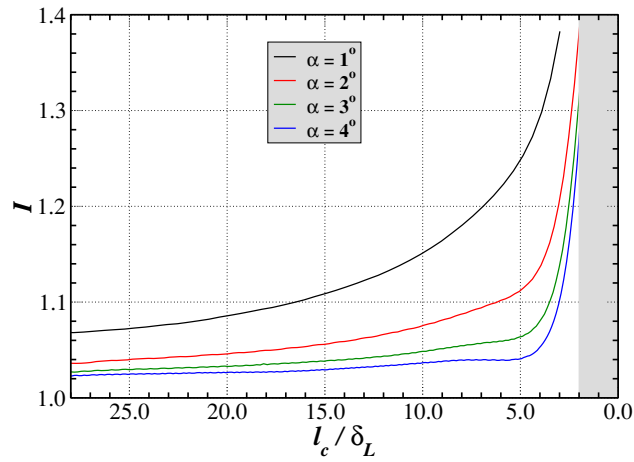


Figure 13 Dependence of the stretch factor, I , given by eq. (23) on the normalized length of the flame-collision region, l_c/δ_L , for four values of α . Shaded gray area indicates the full laminar flame width $2\delta_L$. See text for further details.

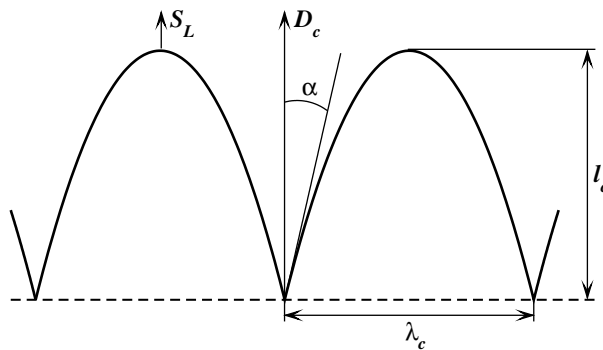


Figure 14 Illustration of the idealized perturbed flame stabilized by the propagation of a cusp with the speed D_c (cf. Fig. 10).

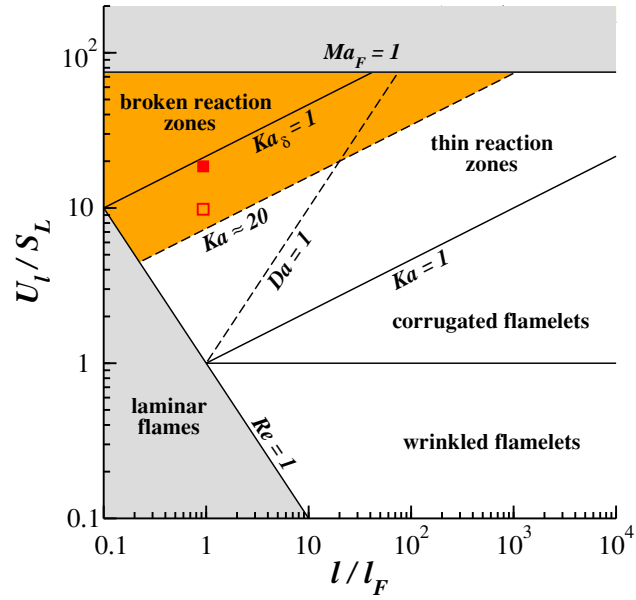


Figure 15 Combustion regime diagram according to [10]. Orange region above the $Ka \approx 20$ line shows the range of the regimes in which the formation of cusps is expected to result in values of l substantially above unity according to the criterion discussed in § 5.5. Filled red square corresponds to the simulations presented in this work, while the open red square shows the regime in which the value of $\bar{l}_{0.15} \approx 1.16$ was determined. Flamelets are typically suggested to exist in the regimes below the $Ka_\delta = 1$ line [10]. The traditional form of the diagram was also modified by adding the $Ma_F = U(\gamma P_0/\rho_0)^{-1/2} = 1$ line indicating the region of supersonic turbulence in the cold H_2 -air fuel under the atmospheric conditions. See text for further details.

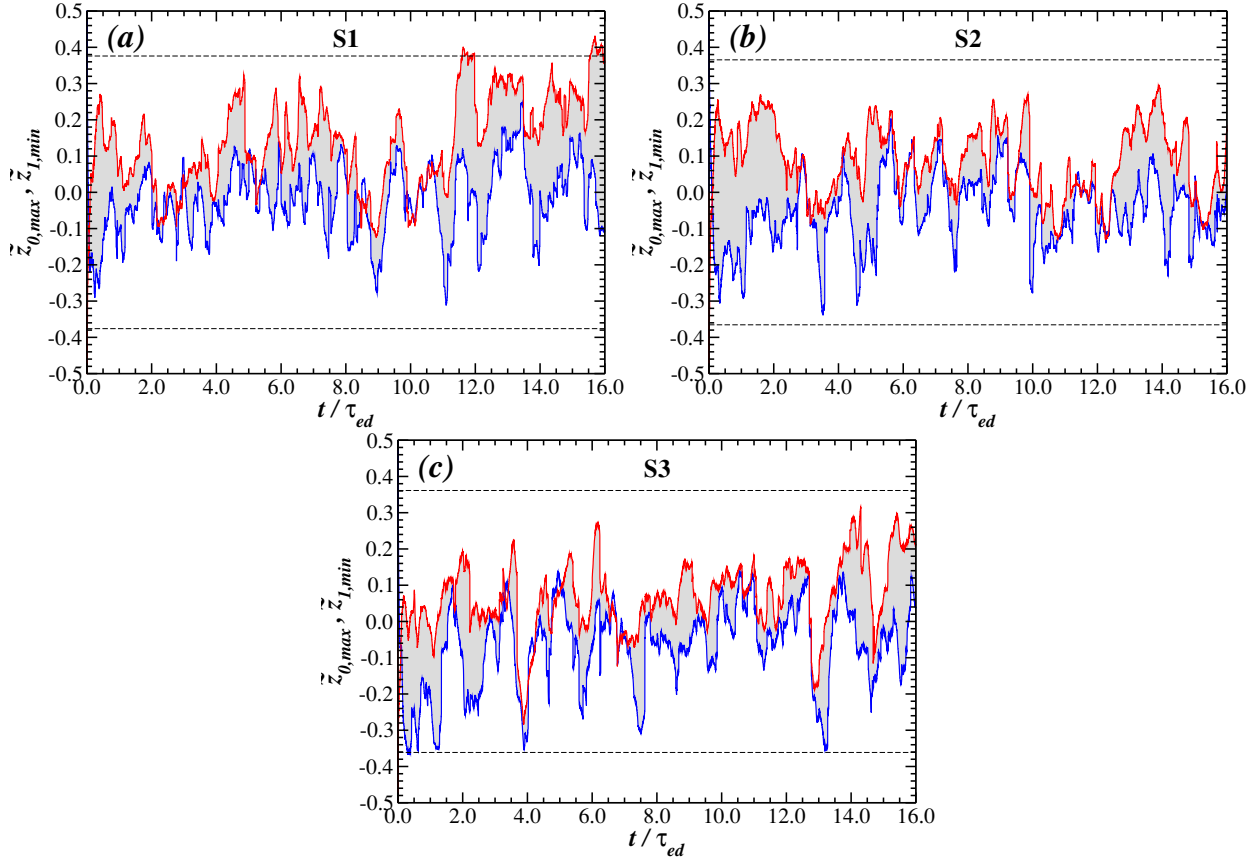


Figure 16 Evolution of the normalized maximum extents of product and fuel penetration into the flame brush $\bar{z}_{0,max}$ and $\bar{z}_{1,min}$ (see text for the definition and Fig. 2 for the illustration) for simulation S1 (a), S2 (b), and S3 (c). $\bar{z}_{0,max}$ is shown with red line, $\bar{z}_{1,min}$ – with blue line. Shaded regions mark the extent of macroscopic mixing of pure fuel and product inside the flame brush. Horizontal dashed lines show the average limiting values of $\bar{z}_{0,max}$ and $\bar{z}_{1,min}$ given by the condition (39) and calculated using the values of $\bar{\delta}_T/\bar{\delta}_L$ listed in Table 3.

